All-day global cloud physical properties products with 0.07° resolution retrieved from geostationary satellite imagers covering the period from 2000 to 2022

Lingxiao Zhao[1], Feng Zhang[1], Zhijun Zhao[1], Feng Lu[2], Jingwei Li[1], Bin Guo[3], and Wenwen Li[4]

[1]Key Laboratory of Polar Atmosphere-Ocean-Ice System for Weather and Climate of Ministry of Education / Shanghai Key Laboratory of Ocean-Land-Atmosphere Boundary Dynamics and Climate Change, Department of Atmospheric and Oceanic Sciences & Institutes of Atmospheric Sciences, Fudan University, Shanghai, China
[2]CMA Key Laboratory for Cloud Physics, Weather Modification Center, China Meteorological Administration (CMA), Beijing, China
[3]College of Physics and Electronic Information Engineering, Zhejiang Normal University, Jinhua, China
[4]Engineering Research Center of Optical Instrument and System, the Ministry of Education, Shanghai Key Laboratory of Modern Optical System, University of Shanghai for Science and Technology, Shanghai, China

Correspondence to: Feng Zhang (fengzhang@fudan.edu.cn)

Abstract.

Clouds play a crucial role in the Earth's energy budget and the hydrological cycle. However, differences in the spatiotemporal resolution of satellite sensors and in retrieval algorithms lead to substantial heterogeneity among retrieved cloud products. This~~Therefore, this~~ study is based on global geostationary satellite thermal infrared brightness temperature data from the Gridded Satellite (GridSat-B1) project~~. Therefore, this study~~ and utilises the single-layer cloud retrieval model—small attention-UNet (Cloud-SmaAtUNet)—within the DaYu CLoud Analysis System (DaYu-CLAS)~~single-layer cloud inversion model small attention-UNet (Cloud-SmaAtUNet) within the DaYu Cloud Analysis System (DaYu-CLAS)~~. ~~Based on global geostationary satellite thermal infrared channel brightness temperature data from the Gridded Satellite (GridSat-B1) project, it has~~ Using these data, we retrieved the first set of all-day Global Cloud physical properties Products (GCP), referred to as DaYu-GCP. This dataset achieves a temporal resolution of 3 h, a spatial resolution of 0.07°, and a temporal span of 23 years (2000–2022). The DaYu-GCP includes cloud phase (CLP), cloud top height (CTH), cloud optical thickness (COT), and cloud effective radius (CER), covering all regions between 70°S–70°N ~~in latitude~~ and 180°W–180°E ~~in longitude~~. Evaluation based on the Moderate-resolution Imaging Spectroradiometer (MODIS) official cloud products shows that the annual CLP identification accuracy of DaYu-GCP remains stable at 85% ± 0.7%, while the annual RMSE for CTH, COT, and CER stabilize at 1.50 ± 0.03 km, 10.71 ± 0.15, and 6.75 ± 0.10 μm, respectively. The multi-year variations in accuracy are within 2%, with no evident interannual differences, and the spatiotemporal distributions are continuous. In addition, evaluation based on observations from the Cloud Profiling Radar and the Cloud-Aerosol Lidar with Orthogonal Polarization (CALIOP) indicates that the DaYu-GCP products ~~exhibit no significant day–night differences and maintain high accuracy under both conditions~~ show reasonable day–night consistency for optically thin cloud. Furthermore, the DaYu-GCP products are compared with other global cloud products. Taking the Northern Hemisphere as an example, the interannual variations of cloud cover

frequency (CCF), CTH, COT, and CER retrieved from DaYu-GCP show correlation coefficients of 0.760, 0.486, 0.764, and 0.514 with the ISCCP product, respectively, and 0.444, 0.778, 0.171, and 0.412 with the CLARA-A3 product. The DaYu-GCP dataset, which is stored in the Network Common Data Format (NetCDF), is freely available on the Science Data Bank at https://doi.org/10.57760/sciencedb.26292 (Zhao et al., 2026). The corresponding code can be found at https://github.com/lingxiao-zhao/DaYu-GCP (last access: 25 June 2025).

1 Introduction

Clouds within the Earth–atmosphere system play a vital role in regulating the planetary radiation balance (Wang et al., 2024; Zhang et al., 2025a) and in the global hydrological cycle (Liu et al., 2024; Viggiano et al., 2025). Therefore, obtaining a high-accuracy, long-term global dataset of cloud physical properties is essential for weather forecasting and climate-change research (Shi et al., 2025; Letu et al., 2023; Tang et al., 2025).

Satellite remote sensing is the primary means of obtaining cloud physical properties. Among these platforms, geostationary satellites can continuously monitor approximately one-third of the Earth's surface day and night, providing high-frequency observations at the minute scale for long-term cloud variability studies. For example, the Advanced Geostationary Radiation Imager (AGRI) onboard the FengYun (FY)-4A/B satellites operated by the National Satellite Meteorological Centre of the China Meteorological Administration (NSMC–CMA) (Min et al., 2017; Min et al., 2020), as well as the Advanced Himawari Imager (AHI) onboard the Himawari-8/9 (H8/9) satellites operated by the Japan Aerospace Exploration Agency (JAXA), can monitor East Asia and the Pacific region (Bessho et al., 2016; Iwabuchi et al., 2018). The Spinning Enhanced Visible and Infra-Red Imager (SEVIRI) onboard the Meteosat Second Generation (MSG) satellites operated by the European Organisation for the Exploitation of Meteorological Satellites (EUMETSAT) provides observations over Africa and Europe (Donny Maladji et al., 1997; Coste et al., 2017; Kocaman et al., 2022). The Geostationary Operational Environmental Satellites (GOES)-R series operated by the National Oceanic and Atmospheric Administration (NOAA), including GOES-16 to GOES-19, are equipped with the Advanced Baseline Imager (ABI) to monitor the Americas (Bin et al., 2018, 2019; Bin et al., 2020; Heidinger et al., 2020). These geostationary satellite sensors provide observations every 10–15 min, with spatial resolutions of 0.5–1 km in the visible channels and 2–5 km in the infrared channels. In contrast to geostationary satellites, polar-orbiting satellites, such as the Moderate-resolution Imaging Spectroradiometer (MODIS) onboard Aqua and Terra (Platnick et al., 2015), cannot provide high-frequency continuous observations over a given region; however, since 2000 they have offered observations with higher spatial resolution (0.25–1 km).

As shown in Table 1~~Table 1~~, based on satellite observation data, these sensors all provide official cloud physical characteristics product datasets, such as official products from the AGRI, AHI, ABI, and SEVIRI, as well as datasets from research initiatives like the Cloud Remote Sensing, Atmospheric Radiation and Renewable Energy (CARE). Most include physical characteristics such as cloud phase (CLP), cloud top height (CTH), cloud optical thickness (COT), and cloud effective

radius (CER), with spatial resolutions of 2–5 km and temporal resolutions of 10–15 minutes. However, these are all regional cloud products, and most lack night-time cloud coverage. In addition, channel spectral responses differ among sensors, and the official cloud product algorithms also vary across platforms. For example, the official AHI cloud products are mainly retrieved using the Comprehensive Analysis Program for Cloud Optical Measurement (CAPCOM) multifunctional algorithm

70   system, which integrates multi-channel threshold methods and a dual visible–near-infrared lookup table (LUT) approach. For liquid water clouds, the Mie–Lorenz scattering model is applied (Nakajima and Nakajma, 1995; Kawamoto et al., 2001), while for ice clouds, an extended Voronoi irregular ice crystal scattering model is used (Letu et al., 2020b), enabling daytime cloud detection and the retrieval of COT and CER (Imai and Yoshida, 2016; Mouri et al., 2016). The ABI official products are developed by the GOES-R Algorithm Working Group, which employs LUT-based retrievals constructed from visible and

75   near-infrared radiances during daytime, while nighttime retrievals rely on thermal infrared channels (Walther and Heidinger, 2012; Walther et al., 2013; Minnis and Heck, 2012), ultimately achieving the retrieval of CLP, CTH, COT, and CER (Pavolonis, 2010; Heidinger, 2012). These differences prevent the direct integration of official geostationary satellite cloud products into a spatiotemporally continuous global cloud product.

Although several global cloud physical property datasets have been developed, such as the third edition of the Satellite

80   Application Facility on Climate Monitoring's (CM SAF) cloud, albedo, and surface radiation dataset from Advanced Very High Resolution Radiometer (AVHRR) observations (CLARA-A3), which retrieves cloud amount, CTH, COT, and CER based on AVHRR measurements, its coverage is global but the temporal resolution is limited to 24 h and the spatial resolution to 0.25° (Karlsson et al., 2023b; Karlsson et al., 2023a). The International Satellite Cloud Climatology Project (ISCCP) uses AVHRR and approximately 10 km geostationary imagery to produce cloud amount, cloud types, cloud top temperature (CTT),

85   and COT products. However, the D series (3 h; 2.5°) (Schiffer and Rossow, 1983; Rossow and Schiffer, 1991; Rossow et al., 1985) and H series (3 h; 1°) (Young et al., 2018; Rossow et al., 2022) were discontinued in 2009 and 2017, respectively. The ~~National Oceanic and Atmospheric Administration~~ National Aeronautics and Space Administration (NASA~~NOAA~~) Satellite ClOud and Radiation Property retrieval System (SatCORPS) employs multiple sensors, such as AHI and SEVIRI, to generate CLP, CTH, COT, and CER products, and although its temporal and spatial resolutions can reach 1 h and 3 km, respectively,

90   the data are currently only available from 2023 onward (Trepte et al., 2019; Yost et al., 2021). These facts indicate that existing global cloud products are unable to simultaneously achieve both long temporal coverage and high spatiotemporal resolution.

Therefore, this study employs the single-layer cloud retrieval model—small attention-UNet (Cloud-SmaAtUNet)—within the DaYu CLoud Analysis System (DaYu-CLAS) to develop an all-day Global Cloud physical properties Products (GCP) retrieval algorithm (DaYu-CLAS) (Zhao et al., 2023, 2024; Tong et al., 2023; J. Li et al., 2023). Further details about the

95   DaYu-CLAS can be accessed at its project website: https://fdu-crias.fudan.edu.cn/. The Cloud-SmaAtUNet model of DaYu-CLAS ~~Therefore, this study employs the single-layer cloud retrieval model small attention-UNet (Cloud-SmaAtUNet) within the DaYu Cloud Analysis System (DaYu-CLAS) to develop an all-day Global Cloud physical properties Products (GCP) retrieval algorithm. The DaYu-CLAS Cloud-SmaAtUNet model~~ takes globally mosaicked thermal infrared channel brightness temperature data from the Gridded Satellite (GridSat-B1) project as input, and is trained using MODIS official cloud products

3

as labels. This approach not only combines the global coverage of the geostationary satellite product GridSat-B1 with the high-precision observation advantages of the polar-orbiting satellite MODIS, but also maximises the extraction of spatial structural information within clouds, thereby enabling all-day, high-accuracy global retrievals of CLP, CTH, CER, and COT products, collectively referred to as DaYu-GCP. The DaYu-GCP products achieve a temporal resolution of 3 h, a spatial resolution of 0.07°, and a time span of 23 years (2000–2022), covering all regions between 70°S–70°N in latitude and 180°W–180°E in longitude, and can provide essential data support for studies of radiative balance, the hydrological cycle, and related processes.

Table 1. Specifications of our DaYu-GCP dataset and the latest cloud physical property product dataset.

Agency	Source	Region	Latitude	Longitude	Products	Spatial resolution	Time resolution	Years (Reference)
Fudan University (DaYu-GCP)	GridSat-B1	Global	70° S–70° N	0° E-360° E	cloud phase, cloud top height, cloud optical thickness, cloud effective radius	0.07°	3 h	2000-2022
National Satellite Meteorological Centre, China Meteorological Administration	FY4A/B-AGRI	China/Full Disc	81° S–81° N	23.8° E-186° E	cloud detection, cloud types, cloud top height, cloud top temperature	4 km	15 min	2018-present (Min et al., 2017; Min et al., 2020)
Aerospace Information Research Institute, Chinese Academy of Sciences (CARE)	FY4A/B-AGRI; H8-AHI	East Asia–Pacific region	60° S–60° N	60° E-180° E	cloud phase, cloud top height, cloud optical thickness, cloud effective radius	0.1°	Daytime: 0.5 h	2016 (Letu et al., 2020a)
National Oceanic and Atmospheric Administration	GOES16/17/18/19-ABI	Western Hemisphere/Full Disc	81° S–81° N	142° E-304° E	cloud phase, cloud top height, cloud optical thickness and cloud effective radius	2 km	1 h	2017–present (Bin et al., 2018, 2019; Bin et al., 2020; Heidinger et al., 2020)
Japan Aerospace Exploration Agency	H8/9-AHI	East Asia–Pacific region	60° S–60° N	80° E-200° E	cloud phase, cloud top height, cloud optical thickness, cloud effective radius	5 km	Daytime: 10 min	2015-present (Bessho et al., 2016; Letu et al., 2016; Iwabuchi et al., 2018)

European Organisation for the Exploitation of Meteorological Satellites	MSG-SEVIRI	European region	81° S–81° N	81° W-81° E	cloud phase, cloud top height (9km), cloud optical thickness, cloud effective radius	3 km	15 min	2013-present (Donny Maladji et al., 1997; Coste et al., 2017; Kocaman et al., 2022)
National Aeronautics and Space Administration (ISCCP)	AVHRR and ~10 km geostationary imagery	Global	90° S–90° N	0° E-360° E	cloud amount, cloud types, cloud top temperature, cloud optical thickness	D: 2.5°	3 h	1983–2009 (Schiffer and Rossow, 1983; Rossow and Schiffer, 1991; Rossow et al., 1985)
						H: 1°	3 h	1983–2017 (Young et al., 2018; Rossow et al., 2022)
European Organisation for the Exploitation of Meteorological Satellites (CLARA-A3)	AVHRR	Global	90° S-90° N	0° E-360° E	cloud amount, cloud top height, cloud optical thickness, cloud effective radius	0.25°	24 h/ 1 month	1979-2020 (Karlsson et al., 2023b; Karlsson et al., 2023a)
National Aeronautics and Space Administration (SatCORPS)	H8-AHI; MSG-SEVIRI; GOES16/17/18/19-ABI; MODIS-Aqua/Terra	Global	90° S-90° N	0° E-360° E	cloud phase, cloud top height, cloud optical thickness, cloud effective radius	3 km	1 h	2023-present (Trepte et al., 2019; Yost et al., 2021)

This paper provides further details on the DaYu-GCP dataset records, including input data, algorithm explanations, product examples, and validation results. Section 2 briefly introduces data preparation and methods, while Section 3 introduces, discusses and evaluates four major products: CLP, CTH, COT and CER. Additionally, DaYu-GCP was compared with existing global cloud datasets ISCCP and CLARA-A3. Section 4 is the conclusion. Section 5 describes the availability of the data.

2 Data and methods

2.1 Data

This study employed two datasets: the geostationary satellite integrated data GridSat-B1 and the polar-orbiting satellite data MODIS. Further details are provided in Table 2~~Table 2~~.

2.1.1. GridSat-B1 data

The primary source of geostationary infrared-channel brightness temperature data used in this study is the GridSat-B1 dataset. Over the 23-year study period (2000–2022), a total of 24 satellites from four countries or regions contributed to the construction of the GridSat-B1 dataset, as shown in Fig. 1. This global dataset integrates observations from multiple geostationary satellites to provide top-of-atmosphere (TOA) infrared brightness temperatures from two bands: the infrared water-vapor band (IRWVP, 6.7 μm) and the infrared window band (IRWIN, 11 μm). In addition to IRWVP and IRWIN, and in consideration of the physical generation mechanisms and developmental processes of clouds, the satellite identifiers (Satid) associated with the infrared brightness temperature data, together with the corresponding satellite zenith (SAZ) angles, have been included in the input data. The parsing procedure for Satid and SAZ in the auxiliary data is described in the GridSat-B1 documentation (Knapp et al., 2011). Additionally, the official documentation indicates that zenith-angle correction for infrared brightness temperature images may be referenced in Joyce et al. (2001). Because the IRWVP and IRWIN grid integrated products may originate from different satellites, Satid is divided into IRWVP satellite identifiers (Satid_VP) and IRWIN satellite identifiers (Satid_IN), and SAZ is similarly separated into IRWVP SAZ (SAZ_VP) and IRWIN SAZ (SAZ_IN). GridSat-B1 has a standard spatial grid resolution of 0.07° and a temporal resolution of 3 h, corresponding to standard synoptic times of 0000, 0300, ..., 2100 UTC. For each grid point, the measurement closest to the satellite nadir is selected. Missing data at these specified times are supplemented from ISCCP (Young et al., 2018) using the temporally nearest available image.
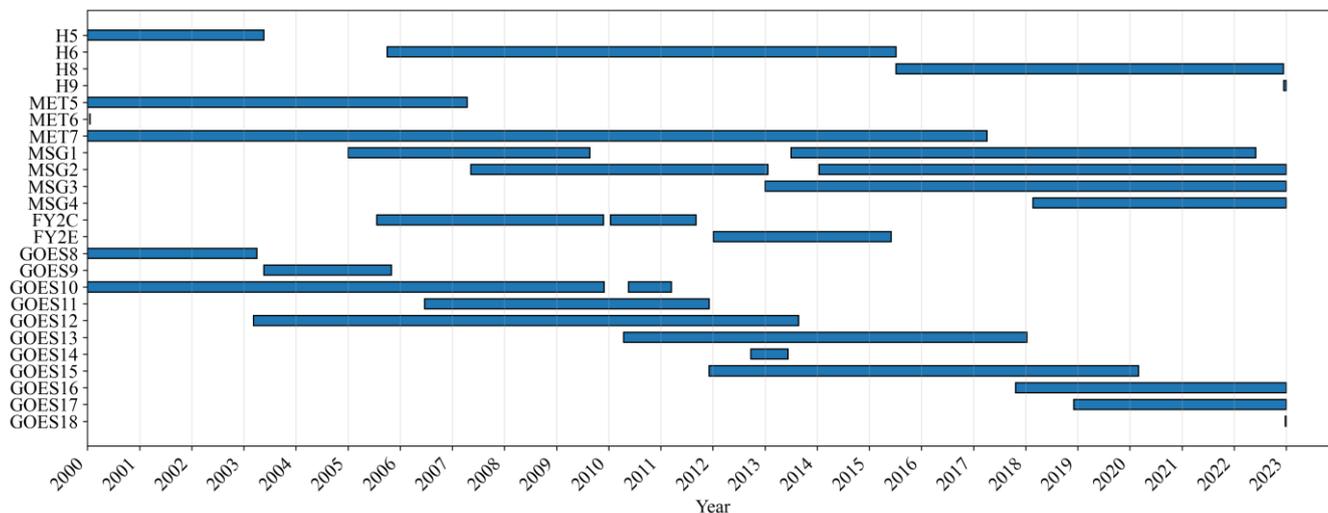
160

Figure 1. Gantt chart of the 24 satellites contributing to the GridSat-B1 project during the study period.

2.1.2. Polar orbit satellite data

The MODIS instrument operates aboard two polar-orbiting satellites: Terra (launched in December 1999) and Aqua (launched
165 in April 2002). With 36 spectral channels and a global revisit frequency of 1–2 days, MODIS's broad spectral coverage
supports a wide range of applications, including vegetation-health monitoring, land-cover classification, sea-surface
temperature retrieval, and cloud analysis (Hosen et al., 2023; Cai et al., 2011; Menzel et al., 2008). In this study, cloud physical
properties from the MODIS Level-2 cloud product (Collection 6.1) were used as training labels, specifically CLP, CTH, CER,
and COT. This product, identified by the code "06", provides data from the Terra platform (MOD06) and the Aqua platform
170 (MYD06). Owing to its well-characterized accuracy and high data quality, the MODIS Collection 6.1 product is widely utilized
as a benchmark in remote-sensing studies (Zhang et al., 2017). The Cloud Profiling Radar and Cloud-Aerosol Lidar with
Orthogonal Polarization (CALIOP) instrument, mounted on the Cloud-Aerosol Lidar and Infrared Pathfinder Satellite
Observation (CALIPSO) satellite, was launched in April 2006 and ceased operations in June 2023 (Winker et al., 2010).
CALIPSO provides global observations of the vertical structure and characteristics of aerosols and thin clouds (Zhang et al.,
175 2017; Hagihara et al., 2010). The assessment of model accuracy primarily utilized official cloud products from MODIS and
CALIOP.

The CLP, CTH, COT, and CER selected from the MODIS official cloud products in this study originate from the
Cloud_Phase_Infrared_1km, cloud_top_height_1km, Cloud_Optical_Thickness, and Cloud_Effective_Radius variables
respectively. The CLP, CTH, and COT from the CALIOP official cloud product are derived from the
180 Feature_Classification_Flags, Layer_Top_Altitude, and Column_Optical_Depth_Cloud_532 variables respectively.

7

2.1.3. ERA5 data

Meteorological field data are obtained from the European Centre for Medium-Range Weather Forecasts (ECMWF) Reanalysis v5 (ERA5) dataset (Hersbach et al., 2020). This study selected ERA5 hourly air temperature profiles (ATP), relative humidity profiles (RHP), skin temperature (SKT), total column water vapor (TCWV) and land cover with a spatial resolution of 0.25°. Excessively dense pressure levels in the input data may introduce unnecessary model redundancy and adversely affect training and operational efficiency. Therefore, ATP and RHP were each extracted at four identical pressure levels: 1000, 850, 500, and 300 hPa (Zhao et al., 2024; Liu et al., 2025).

Table 2. Input, target and evaluation data preparation for building the dataset.

|	Variable	Source	Spatial resolution	Temporal resolution
Input	TOA Brightness Temperature (2 bands: IRWVP 6.7 and IRWIN 11 μm) Satellite Zenith Angle (SAZ_VP and SAZ_IN) Satellite Index (Satid_VP and Satid_IN)	GridSat-B1	8 km	3 h
	Skin Temperature Total Column Water Vapor Air Temperature Profile (4 pressure levels: 1000, 850, 500, and 300 hPa) Relative Humidity Profile (4 pressure levels: 1000, 850, 500, and 300 hPa) Land Cover	ERA5	0.25°	1 h
Target	Cloud Phase Cloud Top Height Cloud Optical Thickness Cloud Effective Radius	Aqua and Terra/MODIS	1 km	5 min
Evaluation	Cloud Phase Cloud Top Height Cloud Optical Thickness	CALIPSO/CALIOP	1 km	/

8

2.2 Method

~~In our previous studies, the single-layer and double-layer cloud retrieval models within the DaYu CLoud Analysis System (DaYu-CLAS) have been demonstrated to perform well in all-day cloud physical properties retrievals. (Xiao et al., 2025a)(Yang et al., 2026)DaYu-CLAS includes single-layer cloud retrieval models such as Cloud-ResUNet (Zhao et al., 2023; Zhao et al., 2024; Tong et al., 2023), Cloud-SmaAtUNet (Li et al., 2023a), and the CloudDiff model (Xiao et al., 2025b), as well as the double-layer cloud retrieval model OverlapCloudDiff (Li et al., 2025). Cloud-SmaAtUNet is an improved version of UNet, in which depthwise separable convolutions and convolutional block attention modules (CBAM) are integrated into both the encoder and decoder paths. Li et al. (2023a) applied Cloud-SmaAtUNet to H8-AHI data and demonstrated that Cloud-SmaAtUNet achieves high accuracy and efficiency in cloud physical properties retrieval tasks. However, that study focused on a single sensor and produced cloud products for only one year (2017), which is insufficient to support studies of global cloud physical properties at high spatiotemporal resolution.~~ In our earlier work, we introduced the DaYu Cloud-Radiation-Precipitation analysis Systems (DaYu-CRPS), which includes three core components: the DaYu Radiative Transfer Model (DaYu-RTM) (Zhang et al., 2019; W. Li et al., 2020, 2023; Cai et al., 2023, 2025; Wu et al., 2026), the DaYu-CLAS (Zhao et al., 2023, 2024; Tong et al., 2023; J. Li et al., 2023; Xiao et al., 2025b; W. Li et al., 2022, 2024), and the DaYu PRecipitation Analysis System (DaYu-PRAS) (Xiao et al., 2025a; Yang et al., 2026). The DaYu-RTM is dedicated to simulating the imager measurements and radiative transfer calculations. DaYu-CLAS integrates both single-layer and double-layer cloud retrieval models. DaYu-PRAS incorporates the TPWDiff-CB and RePPIC-Net models for precipitation monitoring and nowcasting. Specifically, the DaYu-CLAS framework integrates several single-layer cloud retrieval models, including Cloud-ResUNet (Zhao et al., 2023, 2024; Tong et al., 2023), Cloud-SmaAtUNet (J. Li et al., 2023), CloudDiff (Xiao et al., 2025b). For double-layer cloud retrieval, it employs two models: Overlap-CloudDiff (J. Li et al., 2025) and a hybrid algorithm that combines DaYu-RTM simulation with deep learning (W. Li et al., 2022, 2024). Cloud-SmaAtUNet is an improved version of UNet, in which depthwise separable convolutions and convolutional block attention modules (CBAM) are integrated into both the encoder and decoder paths. J. Li et al. (2023) applied Cloud-SmaAtUNet to H8-AHI data and demonstrated that Cloud-SmaAtUNet achieves high accuracy and efficiency in cloud physical properties retrieval tasks. However, that study focused on a single sensor and produced cloud products for only one year (2017), which is insufficient to support studies of global cloud physical properties at high spatiotemporal resolution.

Therefore, in this study, the Cloud-SmaAtUNet model is applied to achieve global all-day cloud physical properties retrievals, as shown in Fig. 2. Due to the different institutional sources of the datasets, they may have different projection methods and spatiotemporal resolutions. To ensure the correct correspondence of pixels and data consistency, the data were first aligned to a unified 0.07° latitude and longitude grid before model construction. Temporal matching was conducted based on the respective temporal characteristics of the datasets. MODIS and ERA5 data, available at synoptic hours (0000, 0300, ..., 2100 UTC), were directly matched. In contrast, CALIOP data, were included by selecting profiles within a ±2 min window

225 around each corresponding synoptic hour. Because the GridSat-B1 images are too large to be directly used as model inputs, each image is divided into multiple 64 × 64 pixel sub-images. After data preprocessing, Cloud-SmaAtUNet is trained using brightness temperature (BT) from the 6.7 and 11 μm channels and the SAZ as the primary inputs, with CLP, CTH, COT, and CER from the MODIS official cloud products as labels. Considering the influence of meteorological conditions on cloud formation and development, additional meteorological variables, such as temperature and humidity profiles, are incorporated

230 as auxiliary inputs. In this way, a DaYu-GCP dataset with a temporal resolution of 3 h and a spatial resolution of 0.07° is retrieved. Finally, the products are validated using the MODIS and CALIOP official cloud products to evaluate their spatiotemporal continuity and day–night consistency.
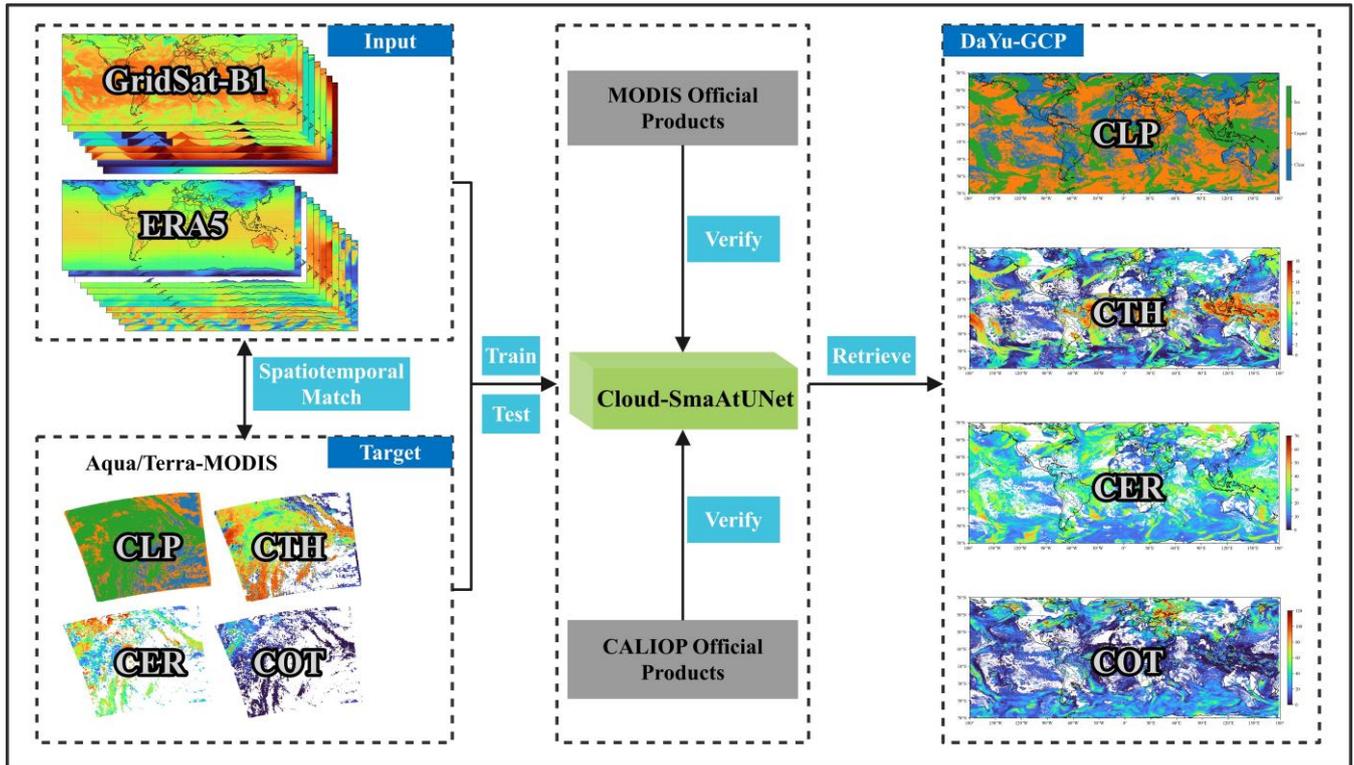
235 **Figure 2.** Flowchart of DaYu-GCP production. It is worth noting that the input data consists of 19 channels, including GridSat-B1 and ERA5, while the target is CLP, CTH, COT, and CER images from MODIS official product processed to the same resolution. The training input and output image sizes are both 64×64. For each target, this study conducted model training and validation and evaluation separately. Finally, a sliding window fusion strategy was used to produce global-scale cloud product data.

240 During model parameter training, the spatiotemporally matched dataset comprised approximately 700,000 sample pairs. Data spanning 2000–2021 were used as the training set, while the entire dataset from 2022 constituted the testing set. These samples were evenly distributed across the spatial domain, and the strategy for selecting the training and testing sets satisfied the basic requirements of Cloud-SmaAtUNet. This selection strategy, together with the large overall sample size, jointly

10

reduces the risk of model overfitting. To further expand the training data, data augmentation operations—including horizontal flipping, vertical flipping, and rotations of 90°, 180°, and 270°—were applied to the training set, increasing its size to six times the original. Meanwhile, the testing set remained unchanged, without any augmentation, in order to objectively evaluate the effectiveness of data augmentation in improving model performance. Indeed, the application of data augmentation led to improved accuracy. Detailed information on the dataset is provided in Table 3Table 3.

Table 3. Sample size and division of the matched dataset into training-set and testing-set.

Data matching pair	Total number of samples	Training -set	Testing- set	Training-set (data augmentation)	Testing-set (data augmentation)
GridSat-B1 & MOD06 Labels	373269	357744	15525	2146464	15525
GridSat-B1 & MYD06 Labels	324950	312090	12860	1872540	12860
Combined MOD06 & MYD06 Labels	698219	669834	28385	4019004	28385

Key parameters for model training include: batch size = 512, maximum epochs = 300, and learning rate = 0.001. An early-stopping strategy was adopted, whereby training was terminated if the loss on the testing set did not decrease by more than 0.1 for 15 consecutive epochs. All models converged and stopped before reaching the maximum of 300 epochs. The loss functions used for model training varied by task. CrossEntropyLoss was employed for the CLP classification task, whereas MSELoss was applied to the CTH, COT, and CER regression tasks. To achieve seamless global coverage of the cloud products, an image sliding-window fusion strategy was implemented to eliminate gaps between adjacent small samples; details of this method are provided in Supplementary Material Text S1. For model evaluation, statistical metrics for classification performance included Accuracy, Recall, Precision, and F1-score, while regression performance was assessed using root mean squared error (RMSE), mean absolute error (MAE), mean bias error (MBE), and Pearson correlation coefficients (PearsonR).

3 Results and Discussion

3.1. Evaluation of model performance in testing-set

To enhance the physical interpretability of the model, the pixel-based (point-to-point) cloud retrieval machine learning model Random Forest (Cloud-RF) (Breiman, 2001) was employed as a comparative benchmark. Here, a grid-search approach was used to determine the Cloud-RF model parameters, with n_estimators = 200, max_depth = 50, min_samples_split = 3, and

290 min_samples_leaf = 1. Using the 2022 test dataset, we compared the performance of the Cloud-SmaAtUNet and Cloud-RF models. Compared with the MODIS official products, Cloud-SmaAtUNet achieved an overall accuracy of 82.3% in the CLP classification task. The recognition accuracies of Cloud-SmaAtUNet for clear sky, water clouds, and ice clouds reached 81.52%, 80.21%, and 86.38%, respectively (Fig. 3(a)). In addition, Cloud-SmaAtUNet also exhibited relatively dense joint probability density distributions aligned along the diagonal in the regression tasks for CTH, COT, and CER. Although Cloud-

295 SmaAtUNet showed a systematic underestimation (MBE < 0), the estimation errors for CTH, COT, and CER remained within acceptable ranges (Fig. 3 (c)(e)(g)). The RMSE (MAE) values were 1.617 km (0.954 km), 11.314 (6.871), and 7.181 μm (5.133 μm), respectively, with PearsonR of 0.926, 0.617, and 0.799. These results indicate that Cloud-SmaAtUNet exhibits excellent performance in the retrieval of cloud physical properties.

In contrast, the performance of the Cloud-RF model in cloud retrieval declined across all products. The overall accuracy

300 of Cloud-RF in the CLP classification task decreased to 78.1% (Fig. 3(b)). Among the classes, the recognition accuracy for water clouds decreased most markedly (73.44%), while those for clear sky and ice clouds also showed slight reductions (78.93% and 85.19%, respectively). This indicates that Cloud-RF performs worse than Cloud-SmaAtUNet in CLP classification. Moreover, in the regression tasks for CTH, COT, and CER, Cloud-RF exhibited more pronounced underestimation than Cloud-SmaAtUNet (MBE < 0 with larger magnitude), and the joint probability density distributions aligned along the diagonal were

305 less concentrated (Fig. 3 (d)(f)(h)). The RMSE (MAE) values were 2.369 km (1.483 km), 13.370 (8.935), and 8.860 μm (6.535 μm), respectively, with PearsonR of 0.843, 0.565, and 0.719. These results demonstrate that, compared with Cloud-SmaAtUNet, the Cloud-RF model shows inferior performance in retrieving cloud physical properties.

Compared with the conventional Cloud-RF, Cloud-SmaAtUNet can leverage the spatial structure information of clouds to improve cloud physical properties retrievals. The accuracy of CLP is increased by 5.4%, while the RMSE of CTH, COT,

310 and CER are reduced by 31.7%, 18.2%, and 23.4%, respectively. Beyond the performance differences, Cloud-SmaAtUNet requires only about 100 s to retrieve a single global image, whereas Cloud-RF takes nearly six times longer, approximately 630 s. These findings are also reflected in other studies (Zhao et al., 2024).
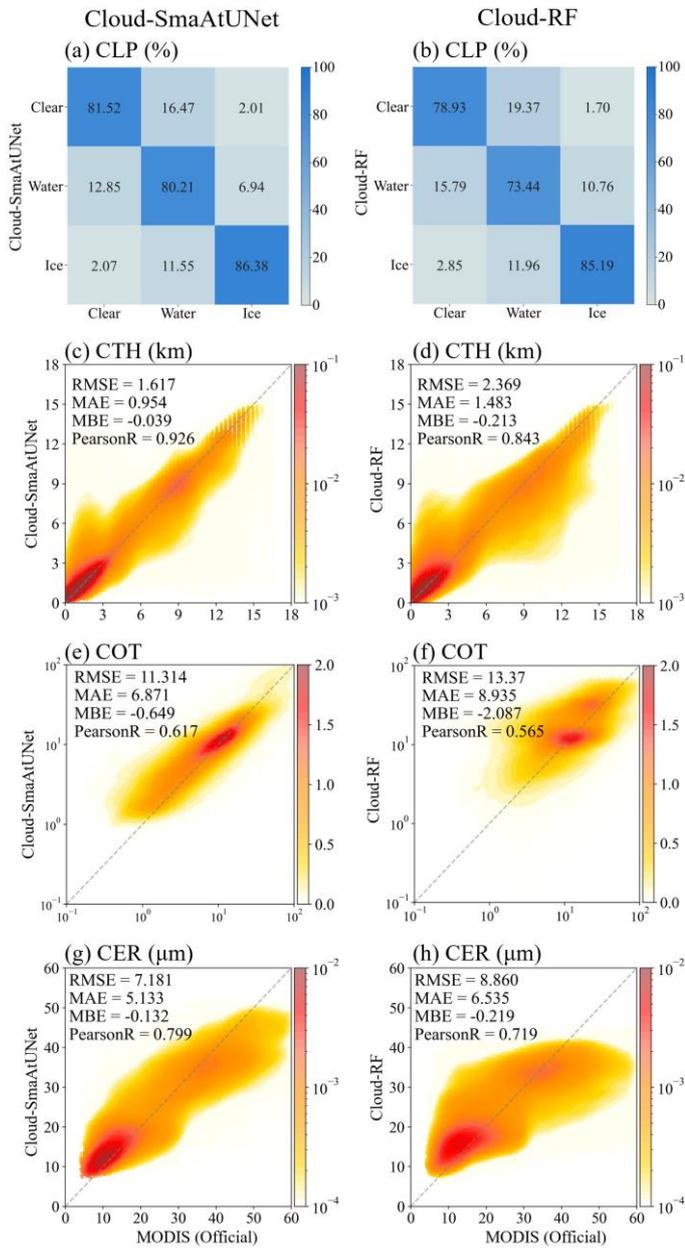
Figure 3. Detailed distribution of testing-set evaluations on Cloud-SmaAtUNet (left column) and Cloud-RF (right column). (a-b) Confusion
matrix for CLP. Scatter density distribution diagram under the kernel density estimation of (c-d) CTH. (e-f) COT. (g-h) CER between
MODIS official and DaYu-CLAS Cloud-SmaAtUNet or DaYu-CLAS Cloud-RF products.

13

3.2. Physical interpretability of the Cloud-SmaAtUNet model

To elucidate the physical interpretability of the model, we investigated the roles of BT and meteorological fields in cloud retrieval. This experiment involved feature ablation testing, comparing model performance across different input combinations (BT only, ERA5 only, BT and ERA5) to analyze each data source's contribution to retrieval accuracy. Specifically, for both the Cloud-SmaAtUNet and Cloud-RF models, three distinct input configurations were employed: Group 1 incorporated 11 μm and 6.7 μm BT along with the full set of ERA5 meteorological fields; Group 2 comprised solely 11 μm and 6.7 μm BT data; Group 3 comprised solely ERA5 meteorological field data. These experiments utilized both Cloud-SmaAtUNet and Cloud-RF models for training and evaluation, with results presented in Table S1 (see Supplementary Materials) and Fig. 4.

The CLP classification results in Table S2 indicate that when using only ERA5, the Cloud-SmaAtUNet classification Accuracy for clear sky, water cloud, and ice cloud were 66.06%, 63.64%, and 68.16%, respectively; when using only BT, the Accuracy was 78.86%, 79.43%, and 83.96%. Using BT and ERA5 together, the classification Accuracy for clear sky, water cloud, and ice cloud improved to 81.52%, 80.21%, and 86.38%, representing increases of 23.4%, 26.0%, and 26.7% compared to using ERA5 alone, and increases of ~~3~~19.4%, ~~1.0~~24.8%, and ~~2.9~~23.2% compared to using BT alone.

The results of the regression tasks are shown in Fig. 4. When using ERA5 alone, the RMSE of CTH, COT, and CER retrieved by Cloud-SmaAtUNet across different ranges were 2.1–7.2 km, 12.9–82.9, and 7.0–25.3 μm, respectively. When using only BT, the RMSE was 1.5–6.0 km, 9.2–63.7, and 4.8–24.1 μm. When using BT and ERA5 together, the RMSE of CTH, COT, and CER decreased to 1.1–5.1 km, 6.0–45.9, and 2.8–21.4 μm. These results indicate that using BT and ERA5 together, compared to using only BT (or only ERA5), reduces the RMSE of CTH, COT, and CER on average by 21.0% (63.5%), 39.5% (90.3%), and 42.6% (85.6%), respectively.

The above experimental results indicate that satellite-observed BT represents an integrated signature of clouds, the atmosphere, and surface types. In the cloud retrieval process based on BT, incorporating atmospheric background fields and surface information contributes to the accurate retrieval of cloud physical properties.
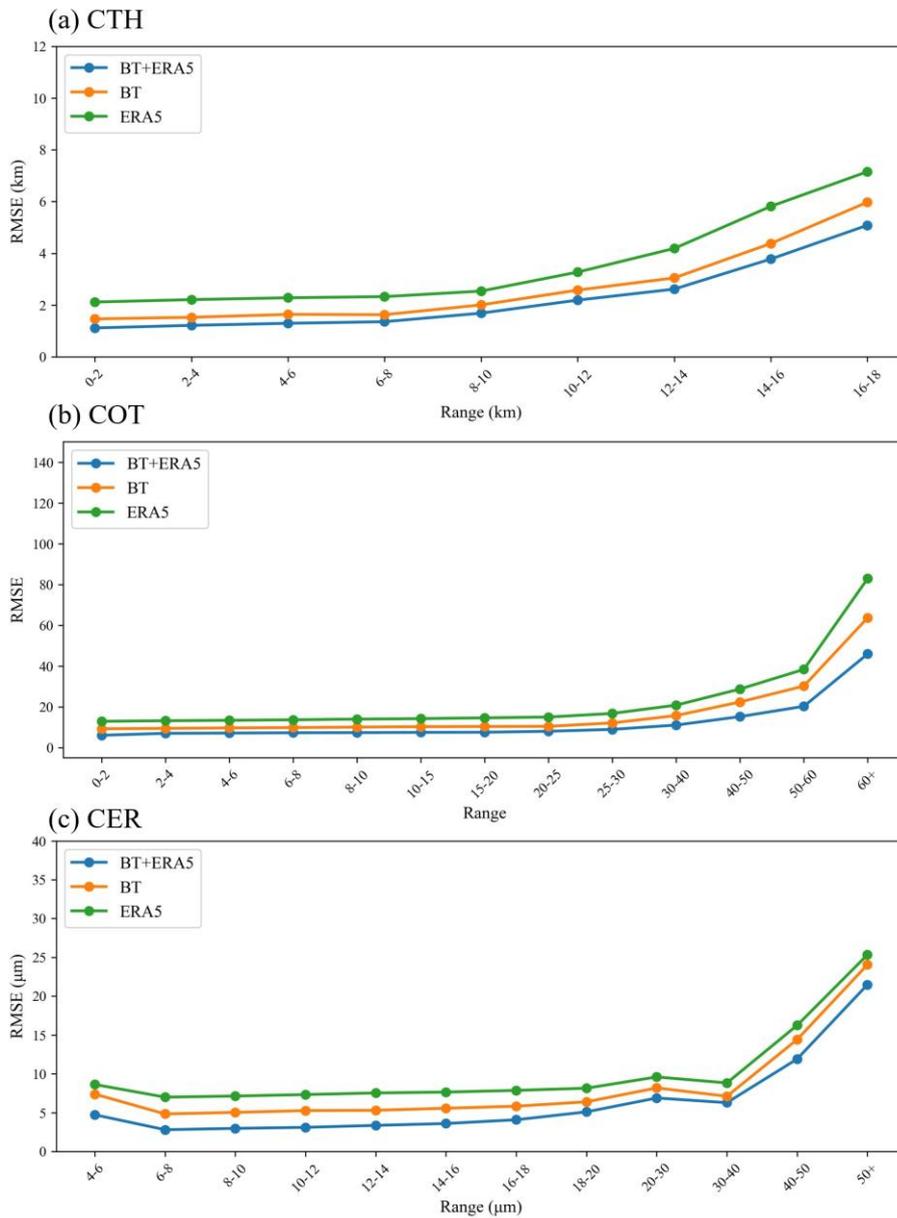
(a) CTH

(b) COT

(c) CER

Figure 4. Cloud-SmaAtUNet ~~(left column) and Cloud-RF (right column) were~~ <u>was</u> evaluated for RMSE across three distinct input datasets, with results presented for different value ranges. Group 1 inputs comprise 11 μm and 6.7 μm BT alongside ERA5. Group 2 inputs comprise 11 μm and 6.7 μm BT. Group 3 inputs comprise ERA5. (a) CTH. (b) COT. (c) CER.

345

3.3. Evaluation of DaYu-GCP with MODIS official products

To assess the interannual stability of the DaYu-GCP products, we validated them using the Aqua/Terra MODIS official cloud products over the period 2000–2022, as shown in Fig. 5. In terms of CLP identification, the Accuracy and Recall for all years are approximately 0.85 ± 0.007. Although there are slight fluctuations in accuracy across years—for example, slightly lower in 2004 and slightly higher in 2010—the differences are minor. This demonstrates that the Cloud-SmaAtUNet model possesses robust cloud detection capability. For the retrievals of CTH, COT, and CER, the annual RMSE values remain stable at 1.50 ± 0.03 km, 10.71 ± 0.15, and 6.75 ± 0.10 μm, respectively, with coefficients of variation (standard deviation/mean) of 2.0%, 1.4%, and 1.5%. These results indicate that DaYu-GCP exhibits stable accuracy across years. The MBE for CTH, COT, and CER across all years range from -0.007 to -0.059 km, -0.536 to -0.649, and -0.069 to -0.283, respectively. Although the MBE deviations are very small, the dataset still exhibits a slight systematic negative bias.
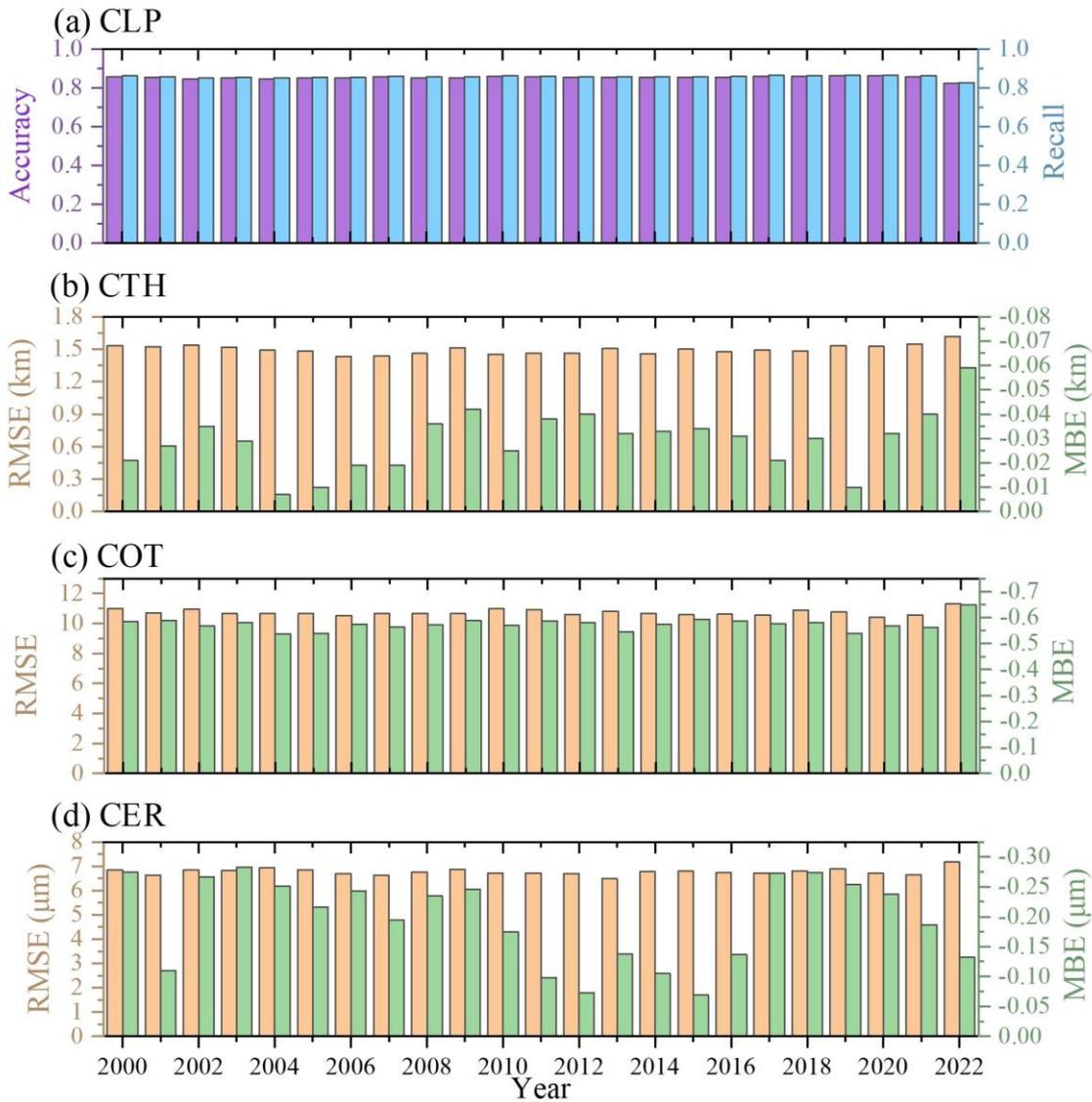
Figure 5. Evaluation of (a) CLP classification accuracy and Recall (b) CTH (bc) COT (cd) CER regression RMSE and MBE results based on training-set and testing-set of Aqua and Terra MODIS official cloud products.

360

We also analyzed the spatiotemporal distribution of spatial discrepancies between DaYu-GCP and MODIS official cloud products from 2000 to 2022. Fig. 6 shows the latitudinal distribution of differences between DaYu-GCP and MODIS official cloud products, with statistical results averaged every 3°. Fig. 7 shows the longitudinal distribution of differences between DaYu-GCP and MODIS official products, with statistical results averaged every 5°. In both Fig. 6 and Fig. 7, the mean values

365   (blue dots), one standard deviation (STD) above and below the mean (blue shading), and box plots (upper bound, lower bound, upper quartile, lower quartile, and median) are presented.

17

Firstly, the latitudinal distribution of CLP exhibits minimal variation, with overall accuracy reaching approximately 0.85. Accuracy increases slightly with increasing latitude. Additionally, the spatial error distributions of CTH and CER in Fig. 6(b) and Fig. 6(d) are relatively consistent, showing higher values near the equator than in other regions. This is primarily because CTH and CER values near the equator are inherently larger, leading to correspondingly larger error margins during model evaluation (Fig. 11(l) and Fig. 11(o)). Mitra et al. (2021) compared MODIS CTH with Lidar observations and found that CTH errors are smaller for low clouds and larger for high clouds. Since cloud heights near the equator are inherently higher, this results in larger errors in CTH retrieval. Zhang et al. (2025b) also found that in equatorial and low-latitude regions, the high mixing of ice and water clouds and complex infrared absorption patterns lead to higher CER values, which in turn result in larger errors during model evaluation. Finally, as shown in Fig. 6(c), COT errors are smaller near the equator and gradually increase with latitude.
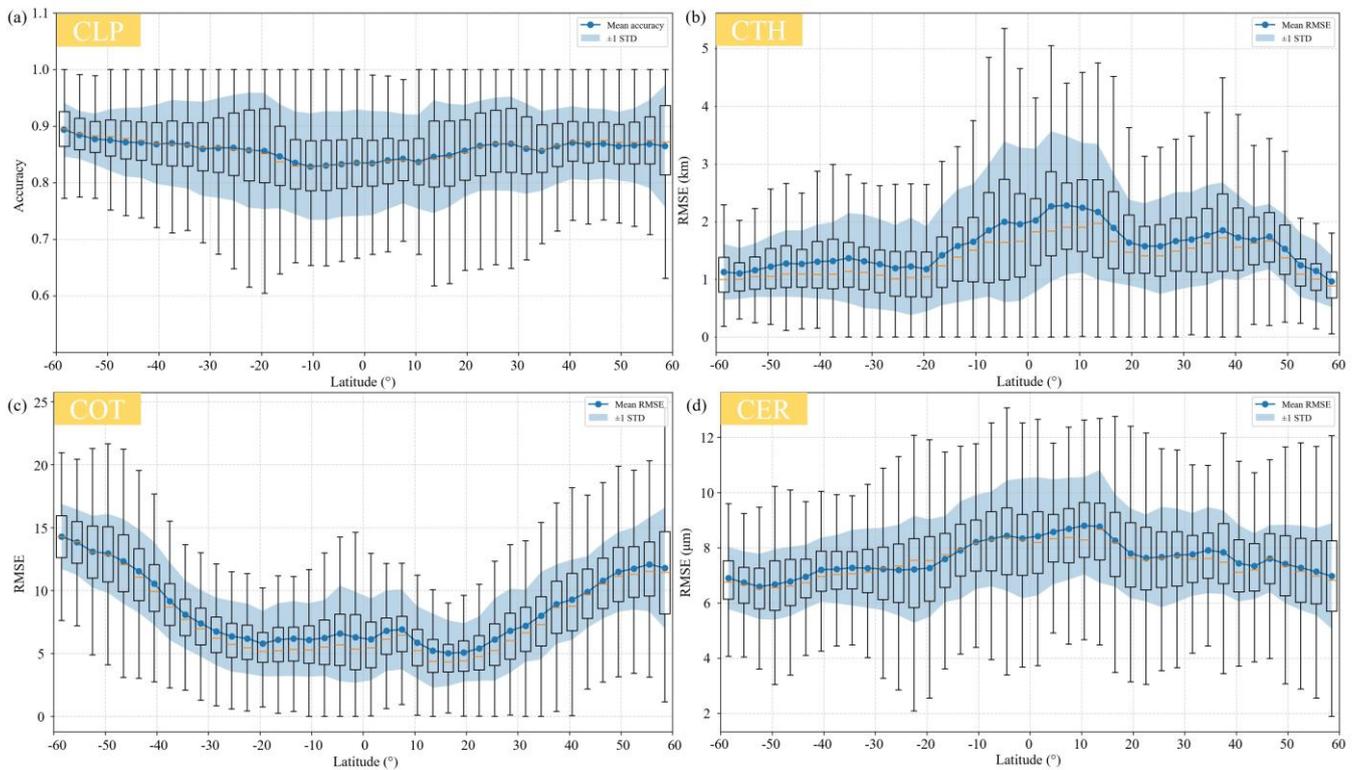
Figure 6. Variation in 23-year average Accuracy and RMSE across different latitudes. (a) CLP. (b) CTH. (c) COT. (d) CER.

Figure 7~~Figure 7~~ shows that for all products, the indicators exhibit clear peak–trough cycles along the longitudinal direction, with the mean Accuracy of CLP fluctuating between 0.82 and 0.88. The mean RMSE of CTH, COT, and CER vary

between 1.3–2.1 km, 7–13, and 6.7–8.2 μm, respectively. This may be because regions with larger fluctuations correspond to fewer samples in the MODIS products, resulting in less stable evaluation results.
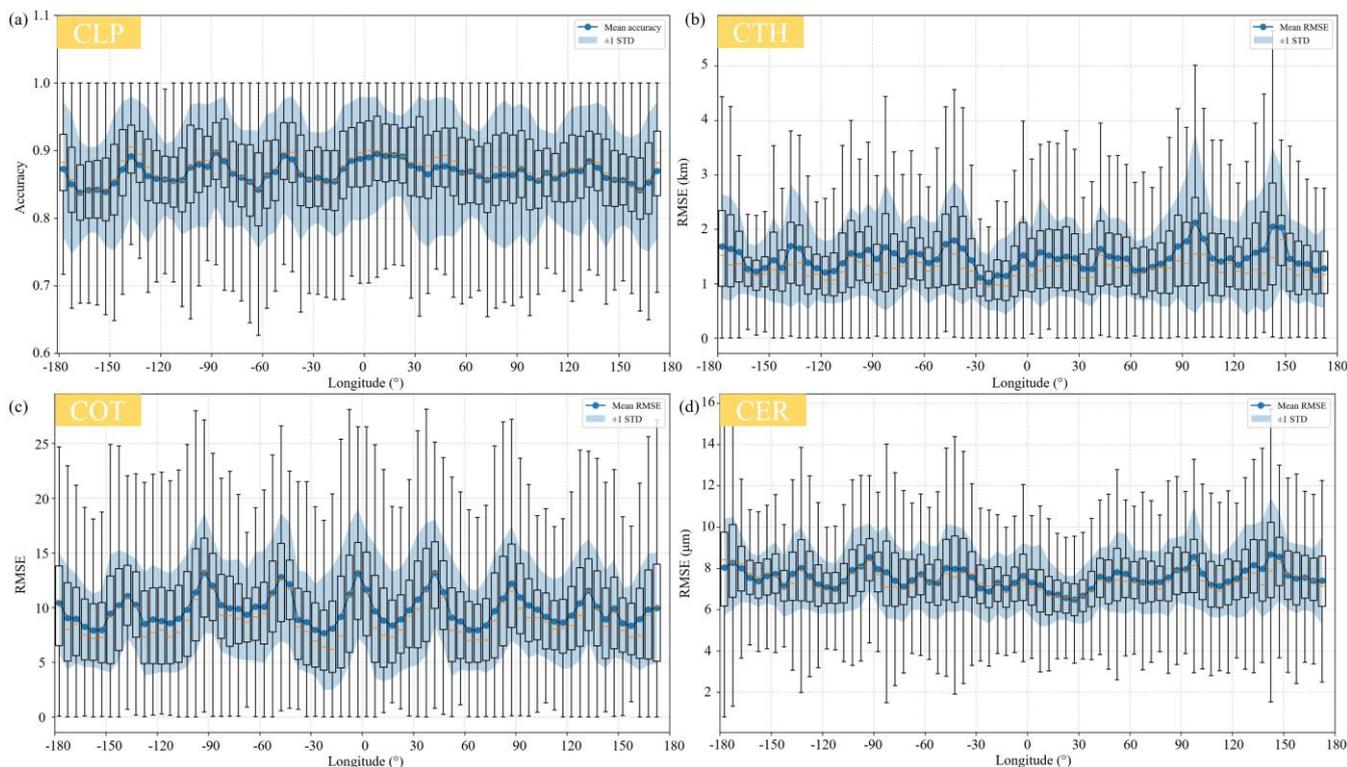

Figure 7. Variation in 23-year average Accuracy and RMSE across different longitudes. (a) CLP. (b) CTH. (c) COT. (d) CER.

3.4. Evaluation of DaYu-GCP with CALIOP official products

In this study, we evaluated the consistency of daytime and nighttime performance of the DaYu-GCP results using CALIPSO/CALIOP data in 2022. Compared with the active sensors CALIPSO/CALIOP, the Accuracy of CLP during the day and night are 0.787 and 0.775, respectively (Fig. 8(a)). The daytime and nighttime RMSE of CTH are 3.384 km and 3.568 km, respectively (Fig. 8(b)). For the evaluation of COT, given that CALIOP cannot penetrate thick cloud layers, this assessment considered only optically thin cloud layers labeled as transparent in the CALIOP data as ground-truth references. Correspondingly, within DaYu-GCP, only optically thin cloud regions with a thickness less than 5 were compared against CALIOP measurements. Finally, the daytime and nighttime RMSE of the COT product are 2.836 and 3.002, respectively (Fig. 8(c)). Overall, the model results demonstrate good consistency between day and night.
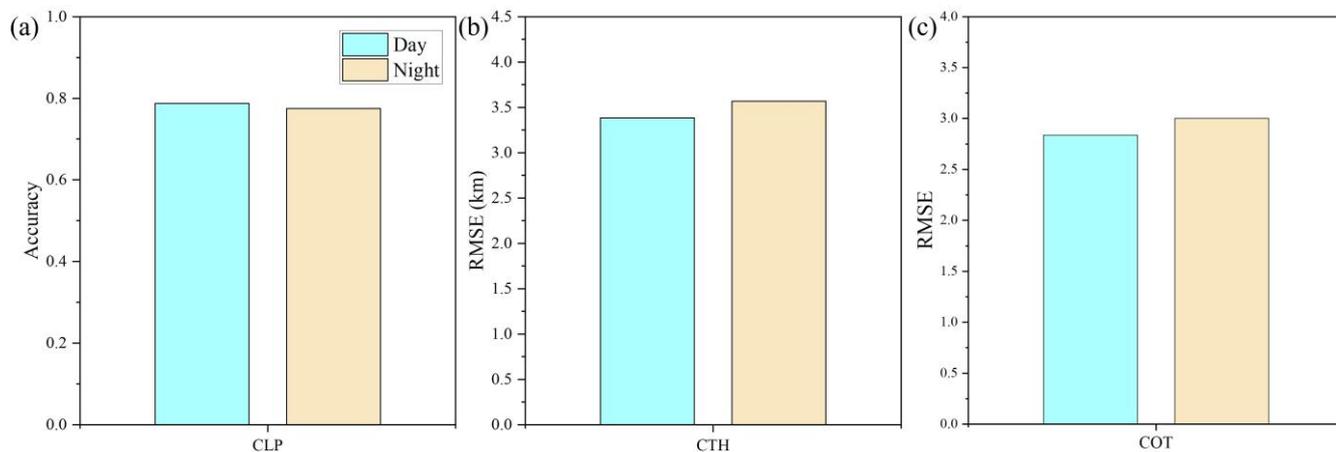
19

Figure 8. The accuracy of the DaYu-GCP (daytime and nighttime) was evaluated using data from the active sensors CALIPSO/CALIOP. (a) CLP accuracy. (b) The RMSE of CTH. (c) The RMSE of COT. The COT evaluation employs optically thin clouds labeled as "transparent" in CALIOP. The blue bar chart shows the model's daytime accuracy, and the yellow bar chart shows the model's nighttime accuracy.

Figure 9Figure 9 presents the validation of DaYu-GCP and MODIS official products against the CALIOP official products for three variables: CLP, CTH, and COT. For CLP, the overall Accuracy of DaYu-GCP shows relatively small variation, with a mean value of approximately 0.76. The Accuracy for clear sky, water clouds, and ice clouds are about 0.74, 0.76, and 0.77, respectively, which are slightly lower than those of MODIS, whose overall Accuracy is around 0.80, with clear sky, water cloud, and ice cloud Accuracy of approximately 0.76, 0.79, and 0.81, respectively. For CTH, the multi-year RMSE of DaYu-GCP ranges from 3.35 to 3.53 km, slightly higher than that of MODIS (3.09–3.32 km). For COT, the multi-year RMSE of DaYu-GCP ranges from 3.59 to 4.08, also slightly higher than MODIS (2.57–3.18). Using the CALIOP official products as the reference, the annual RMSE for CTH and COT remain stable at 3.42 ± 0.15 km and 3.84 ± 0.16, with coefficients of variation of 4.4% and 4.1%, respectively. Overall, the DaYu-GCP products demonstrate stability in both day–night accuracy and interannual variations.
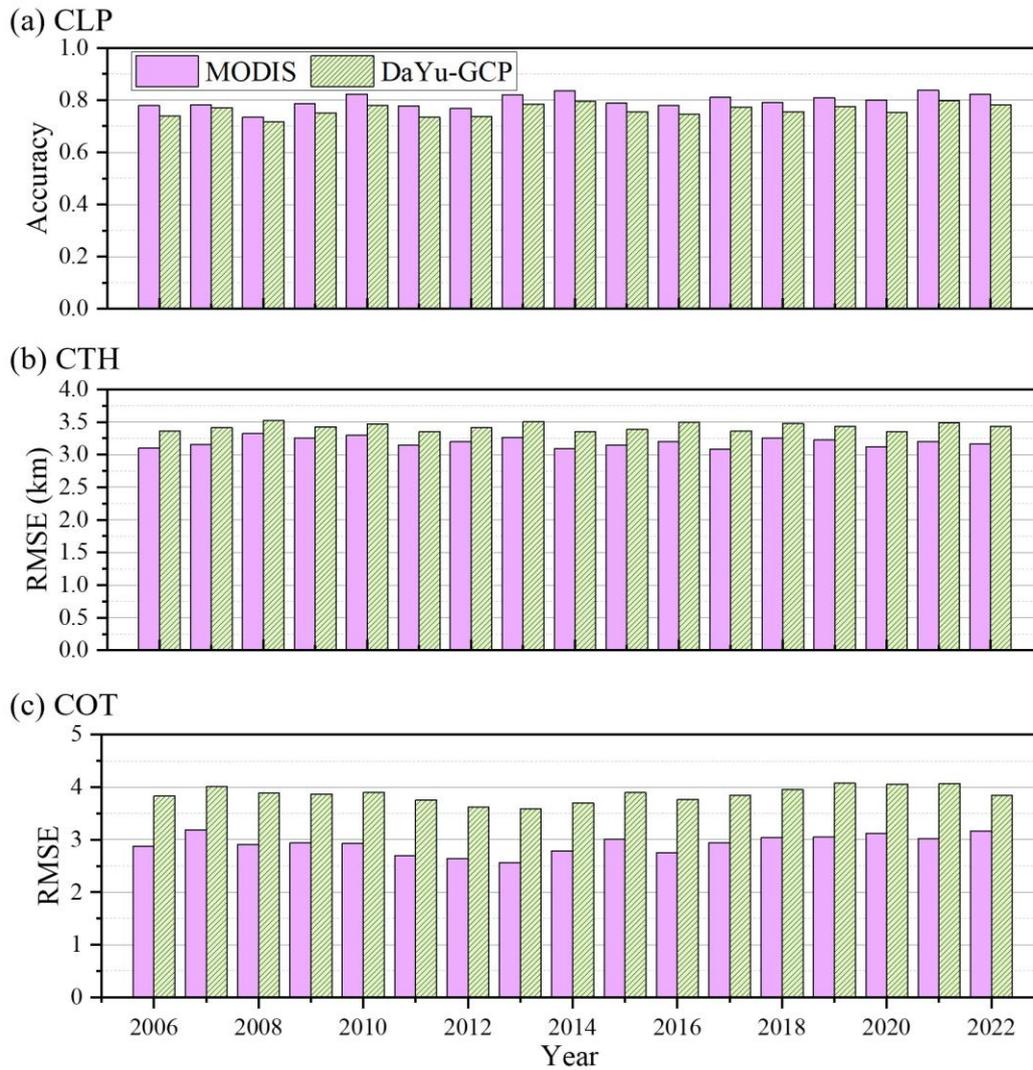
20

Figure 9. Annual evaluation results for MODIS and DaYu-GCP based on CALIOP standards. (a) Comparison of CLP accuracy. (b) Comparison of CTH RMSE. (c) Comparison of COT RMSE. The COT evaluation is restricted to optically thin clouds, defined as CALIOP "transparent" layers and MODIS clouds with COT < 5.

Table 4. The classification accuracy of clear sky, water cloud, and ice cloud for MODIS and DaYu-GCP on an annual basis, using CALIOP as the standard.

Year	MODIS (%)			DaYu-GCP (%)		
	Clear sky	Water cloud	Ice cloud	Clear sky	Water cloud	Ice cloud
2006	76.36	71.77	80.40	74.77	71.58	74.90
2007	82.31	78.84	76.00	81.50	76.53	74.94

21

2008	77.17	75.48	70.86	72.17	74.37	69.34
2009	76.75	76.35	80.43	74.07	76.59	75.01
2010	76.57	80.19	84.52	77.18	76.27	80.03
2011	68.20	76.01	80.17	64.79	79.95	76.02
2012	74.38	77.75	76.80	75.83	74.95	71.28
2013	79.30	81.90	82.76	80.84	77.13	77.58
2014	76.87	80.79	85.84	76.35	78.48	82.34
2015	65.64	77.55	83.65	64.65	77.43	82.28
2016	75.80	77.85	78.62	72.30	74.20	76.05
2017	74.56	81.34	82.59	73.95	76.30	80.10
2018	78.33	80.28	78.57	75.26	78.23	74.33
2019	76.76	82.62	84.63	76.94	77.93	79.69
2020	76.16	82.05	83.15	73.08	76.42	76.32
2021	81.42	83.78	86.83	79.00	78.51	80.99
2022	82.34	81.59	83.81	78.05	80.77	78.46

3.5. Spatiotemporal distribution characteristics of clouds

Since MODIS is carried on polar-orbiting satellites, the spatial coverage of cloud products at any given time is limited, making large-scale, synchronous global observations difficult. Consequently, the spatiotemporal distribution characteristics of the retrieved cloud physical properties lack representativeness.

Here, we initially defined and calculated three physical quantities characterizing cloud cover based on the CLP product: ice cloud fraction (ICF), water cloud fraction (WCF), and total cloud fraction (TCF) (Zhao et al., 2024). To ensure that spatiotemporally matched samples achieve global coverage, this study employed a 1.5 h temporal resolution and used MODIS transit times as the reference for spatiotemporal matching between DaYu-GCP and MODIS data. Monthly and annual average distributions were subsequently calculated.

Annual mean values for each year from 2020 to 2022 are presented in Fig. 10, while the corresponding seasonal means (DJF, MAM, JJA, and SON) are shown in Supplementary Figures S1–S4. Comparison of the results indicates that the MODIS official product and the DaYu-GCP product are highly consistent with respect to ICF, WCF, TCF, CTH, COT, and CER at MODIS transit times (Fig. 10 (a,d,g,j,m,p) and Fig. 10 (b,e,h,k,n,q)), particularly in equatorial regions. Since MODIS transits only at 10:30 AM and 1:30 PM local time, these annual averages do not fully capture the spatiotemporal characteristics of cloud physical properties throughout the day. In contrast, the all-day global DaYu-GCP, which provides complete spatial coverage, compensates for this limitation, representing a significant improvement over the official MODIS products (Fig. 10 (a,d,g,j,m,p) and Fig. 10 (c,f,i,l,o,r)).
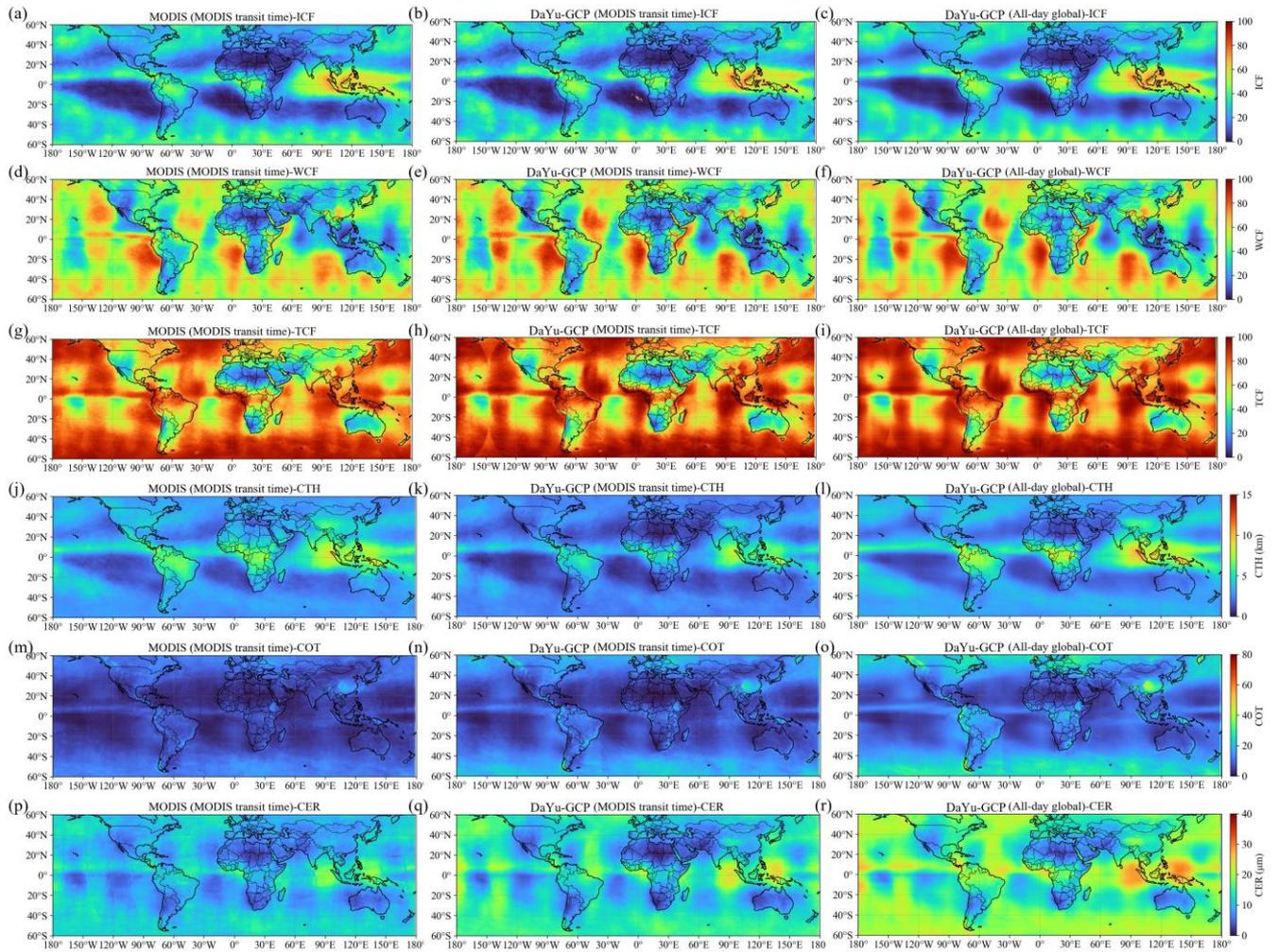
22

Figure 10. Annual average spatial distribution of global cloud physical products from 2020 to 2022, respectively: ICF (a–c), WCF (d–f), TCF (g–i), CTH (j–l), COT (m–o), and CER (p–r). Vertically, these are the averages of the MODIS official cloud products with a 1.5 h transit time interval (a, d, g, j, m, p), the averages of DaYu-GCP at the same MODIS transit time and coverage location (b, e, h, k, n, q), and the averages of DaYu-GCP's all-day global products at all times (c, f, i, l, o, r).

Additionally, DaYu-GCP was compared with the global cloud datasets ISCCP and CLARA-A3. The four variables involved in the comparison were CCF, CTH, CER, and COT. For ISCCP, the base HGG data itself provides global 3 h CCF and COT. CTH can be derived from the provided CTT, and CER can be calculated from the available COT and cloud water path (CWP) (Schiffer and Rossow, 1983; Rossow et al., 1996; Young et al., 2018). For CLARA-A3, the dataset provides global daily mean CCF and CTH directly, whereas COT and CER can be derived from ice water path (IWP) and liquid water path (LWP) (Nakajima and King, 1990).

To clearly compare the annual variability of cloud physical properties among different products, monthly anomaly time series of each parameter were constructed for the Northern and Southern Hemispheres based on the monthly mean data from each product, and Pearson correlation coefficients (R) between DaYu-GCP and the other two datasets were calculated (Fig. 11). DaYu-GCP exhibits higher correlations with ISCCP in CCF, COT, and CER; for the Northern Hemisphere, the R reach 0.760, 0.764, and 0.514, respectively. DaYu-GCP shows higher correlation with CLARA-A3 in CTH, with R = 0.778 for the Northern Hemisphere. The Southern Hemisphere exhibits similar results. Among all R values, CER shows the lowest correlation compared to CCF and CTH; for the Northern Hemisphere, R values between DaYu-GCP and ISCCP, DaYu-GCP and CLARA-A3, and ISCCP and CLARA-A3 are 0.514, 0.412, and 0.219, respectively. This indicates that CER remains a challenging parameter in future cloud physical properties datasets. These comparison results demonstrate that, as a new cloud product, DaYu-GCP exhibits reasonable consistency in the spatiotemporal variability of major cloud parameters with the two long-standing global datasets, ISCCP and CLARA-A3. This underscores the reliable data quality of DaYu-GCP and its potential as a consistent data source for global cloud-climate studies.
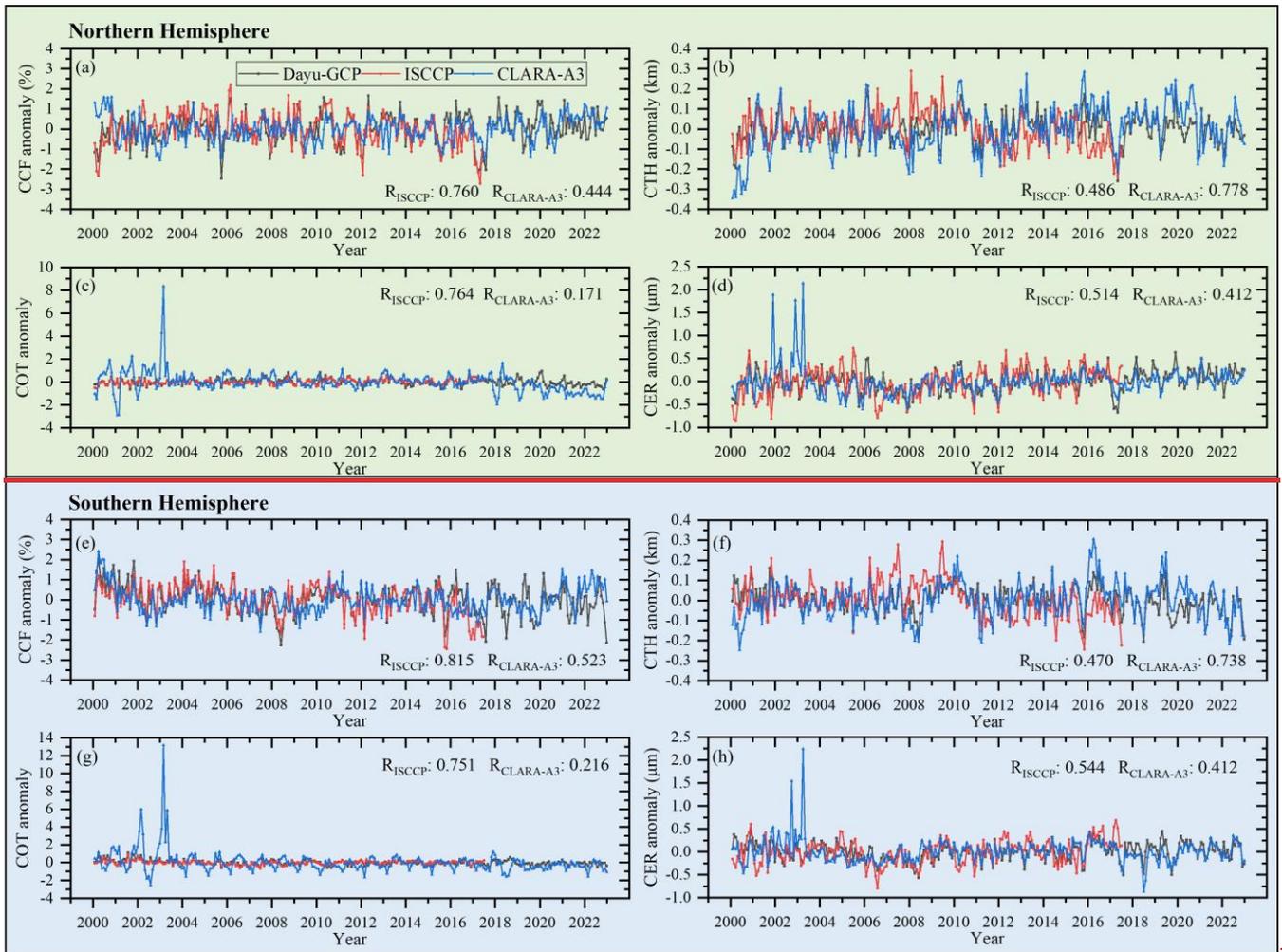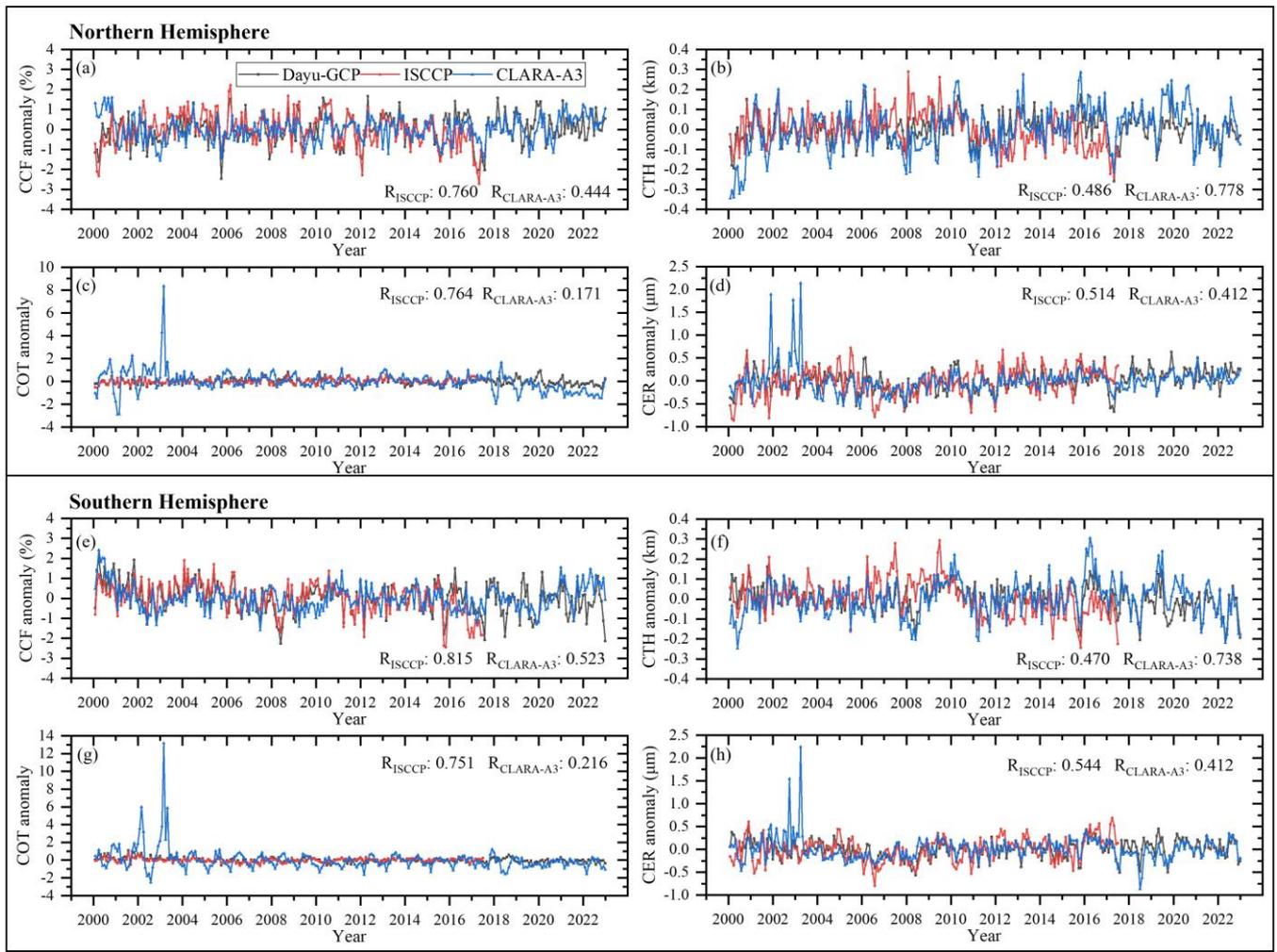
Figure 11. CCF, CTH, COT and CER anomaly change curves for the period 2000 to 2022 across the 60°N to 60°S latitude zone, derived from DaYu-GCP, ISCCP and CLARA-A3 products. Statistical data are presented separately for the Northern and Southern Hemispheres. The black, red and blue curves represent DaYu-GCP, ISCCP and CLARA-A3 respectively. In the corner, we have labelled the Pearson correlation coefficients R_{ISCCP} and $R_{CLARA-A3}$. R_{ISCCP} denotes the correlation coefficient between DaYu-GCP and ISCCP. $R_{CLARA-A3}$ denotes the correlation coefficient between DaYu-GCP and CLARA-A3. (a) and (e) are CCF variables. (b) and (f) are CTH variables. (c) and (g) are CTH variables. (d) and (h) are CTH variables.

4 Conclusion

This study developed and released the first all-day, high spatiotemporal resolution global cloud physical properties product, DaYu-GCP. The product spans the period from 2000 to 2022, with a temporal resolution of 3 h and a spatial resolution of 0.07°, covering all regions between 70°S and 70°N. It includes four key cloud physical properties: CLP, CTH, COT, and CER.

480 Systematic quality assessments indicate that the DaYu-GCP product demonstrates reliable accuracy, strong stability, and good consistency. The specific conclusions are as follows:

(1) Compared with the MODIS official products, the classification Accuracy of CLP reaches 82.3%, and the RMSE of CTH, COT, and CER are 1.617 km, 11.314, and 7.181 µm, respectively. Interannual evaluations show that the CLP Accuracy remains stable at approximately 0.85 ± 0.007, while the RMSE of CTH, COT, and CER remain stable at 1.50 ± 0.03 km, 10.71

485 ± 0.15, and 6.75 ± 0.10 µm, with coefficients of variation of 2.0%, 1.4%, and 1.5%, respectively. This indicates that the accuracy of DaYu-GCP exhibits no significant interannual differences.

(2) Compared with the CALIOP official products, the day–night Accuracy of CLP are 0.787 and 0.775, respectively; the day–night RMSE of CTH are 3.384 km and 3.568 km, and the day–night RMSE of COT are 2.836 and 3.002 for optically thin cloud. These results demonstrate reasonablegood day–night consistency of the product.

490 (3) The product shows reasonable correlations with ISCCP and CLARA-A3 datasets in both hemispheres. For example, in the Northern Hemisphere, the correlations of CCF and COT with ISCCP are high (R = 0.760 and 0.764), while CTH shows a stronger correlation with CLARA-A3 (R = 0.778). The correlations of CER between DaYu-GCP and ISCCP, DaYu-GCP are slightly lower (R = 0.514 and 0.412), whereas the R between ISCCP and CLARA-A3 themselves is only 0.219, indicating that DaYu-GCP maintains higher spatiotemporal consistency with global cloud products ISCCP and CLARA-A3, although

495 the CER retrieval algorithm still requires further development in future studies.

In summary, DaYu-GCP fills the gap in existing global cloud property products that simultaneously offer high spatiotemporal resolution and long-term coverage. The dataset combines high accuracy, strong stability, and robust consistency, and is publicly accessible, making it a valuable resource for studies of cloud–climate feedbacks and the global energy and water cycles. Furthermore, additional research is required in the future to explore how to enhance the data for cloud physical

500 property products in the polar regions and continuously improve observational capabilities to obtain more reliable COT and CER products., thereby obtaining more reliable CER products.

5 Data availability

The DaYu-GCP data described in this paper have been made publicly available. We would like to express our special thanks

505 to Science Data Bank and its staff for their help and support in the data publication process. DaYu-GCP can be accessed at https://doi.org/10.57760/sciencedb.26292 (Zhao et al., 2026). Moreover, the matching dataset employed to train the models in this study is also publicly available and can be accessed at https://doi.org/10.57760/sciencedb.27171 (Zhao, 2025).

Author contribution

510 LZ contributed to conceptualization, methodology, writing–original draft, investigation, validation, data curation, drawing. FZ contributed to supervision, writing-review & editing, funding acquisition. ZZ contributed to investigation, discussion, writing-review & editing. FL contributed to supervision, discussion. JL contributed to investigation, validation. BG contributed to discussion, writing-review & editing. WL contributed to discussion, investigation. All authors reviewed the manuscript.

515 ## Competing interests

The authors declare that they have no conflict of interest.

References

Bessho, K., Date, K., Hayashi, M., Ikeda, A., Imai, T., Inoue, H., Kumagai, Y., Miyakawa, T., Murata, H., Ohno, T., Okuyama,
520 A., Oyama, R., Sasaki, Y., Shimazu, Y., Shimoji, K., Sumida, Y., Suzuki, M., Taniguchi, H., Tsuchiyama, H., Uesawa, D., Yokota, H., and Yoshida, R.: An Introduction to Himawari-8/9—Japan's New-Generation Geostationary Meteorological Satellites, J. Meteorol. Soc. Jpn., 94, 151–183, 2016.

Bin, T., John, D., Robert, W., and Alan, R.: GOES-16 ABI navigation assessment, Proc. SPIE, 107640G, https://doi.org/10.1117/12.2321170, 2018.

525 Bin, T., John, D., Robert, W., and Alan, R.: GOES-16 and GOES-17 ABI INR assessment, Proc. SPIE, 111271D, https://doi.org/10.1117/12.2529336, 2019.

Bin, T., John, J. D., Christopher, N. F., Thomas, J. G., Scott, H., Peter, J. I., Patrick, D. J., Brian, C. P., Alan, D. R., Pradeep, T., and Robert, E. W.: GOES-R series image navigation and registration performance assessment tool set, J. Appl. Remote Sens., 14, 032405, https://doi.org/10.1117/1.JRS.14.032405, 2020.

530 Breiman, L.: Random Forests, Mach. Learn., 45, 5–32, https://doi.org/10.1023/A:1010933404324, 2001.

Cai, H., Zhang, S., Bu, K., Yang, J., and Chang, L.: Integrating geographical data and phenological characteristics derived from MODIS data for improving land cover mapping, J. Geogr. Sci., 21, 705–718, https://doi.org/10.1007/s11442-011-0874-1, 2011.

Cai, Y., Zhang, F., Li, J., Wu, K., and Yang, Q.: An Accurate Shortwave Gaseous Transmittance Scheme Using Modified
535 Alternate Mapping Correlated K-Distribution Method, J. Geophys. Res. Atmos., 130, e2024JD041921, https://doi.org/10.1029/2024JD041921, 2025.

Cai, Y., Zhang, F., Lin, H., Li, J., Zhang, H., Li, W., and Hu, S.: Optimized Alternate Mapping Correlated K-Distribution Method for Atmospheric Longwave Radiative Transfer, J. Adv. Model. Earth Syst., 15, e2022MS003419, https://doi.org/10.1029/2022MS003419, 2023.

540 Coste, P., Pasternak, F., Faure, F., Jacquet, B., Bianchi, S., Donny, M. A. A., Luhmann, H. J., Hanson, C., Pili, P., and Fowler, G.: SEVIRI, the imaging radiometer on Meteosat second generation: in-orbit results and first assessment, Proc. SPIE, 105680L, https://doi.org/10.1117/12.2308023, (year not given).

Donny Maladji, A. A., Bernard, J., and Frederick, P.: Characteristics of the Meteosat Second Generation (MSG) radiometer/imager: SEVIRI, Proc. SPIE, 19–31, https://doi.org/10.1117/12.298084, 1997.

545 Hagihara, Y., Okamoto, H., and Yoshida, R.: Development of a combined CloudSat-CALIPSO cloud mask to show global cloud distribution, J. Geophys. Res. Atmos., 115, https://doi.org/10.1029/2009JD012344, 2010.

Heidinger, A. K.: GOES-R Advanced Baseline Imager (ABI) Algorithm Theoretical Basis Document for Cloud Height (Version 3.0). 79 pp., https://www.star.nesdis.noaa.gov/goesr/documents/ATBDs/Baseline/ATBD_GOES-R_Cloud_Height_v3.0_Jul2012.pdf, 2012.

550 Heidinger, A. K., Pavolonis, M. J., Calvert, C., Hoffman, J., Nebuda, S., Straka, W., Walther, A., and Wanzong, S.: Chapter 6 - ABI Cloud Products from the GOES-R Series, in: The GOES-R Series, edited by: Goodman, S. J., Schmit, T. J., Daniels, J., and Redmon, R. J., Elsevier, 43–62, https://doi.org/10.1016/B978-0-12-814327-8.00006-8, 2020.

Hersbach, H., Bell, B., Berrisford, P., Hirahara, S., Horányi, A., Muñoz-Sabater, J., Nicolas, J., Peubey, C., Radu, R., Schepers, D., Simmons, A., Soci, C., Abdalla, S., Abellan, X., Balsamo, G., Bechtold, P., Biavati, G., Bidlot, J., Bonavita, M., De Chiara, 555 G., Dahlgren, P., Dee, D., Diamantakis, M., Dragani, R., Flemming, J., Forbes, R., Fuentes, M., Geer, A., Haimberger, L., Healy, S., Hogan, R. J., Hólm, E., Janisková, M., Keeley, S., Laloyaux, P., Lopez, P., Lupu, C., Radnoti, G., de Rosnay, P., Rozum, I., Vamborg, F., Villaume, S., and Thépaut, J.-N.: The ERA5 global reanalysis, Q. J. R. Meteorol. Soc., 146, 1999–2049, https://doi.org/10.1002/qj.3803, 2020.

Hosen, M. K., Alam, M. S., Chakraborty, T., and Golder, M. R.: Monitoring spatiotemporal and seasonal variation of 560 agricultural drought in Bangladesh using MODIS-derived vegetation health index, J. Earth Syst. Sci., 132, 188, https://doi.org/10.1007/s12040-023-02200-3, 2023.

Imai, T. and Yoshida, R.: Algorithm Theoretical Basis for Himawari-8 Cloud Mask Product, Meteorological Satellite Center Technical Note, 61, 1–17, https://www.data.jma.go.jp/mscweb/technotes/msctechrep61-1.pdf, 2016.

Iwabuchi, H., Putri, N. S., Saito, M., Tokoro, Y., Sekiguchi, M., Yang, P., and Baum, B. A.: Cloud Property Retrieval from 565 Multiband Infrared Measurements by Himawari-8, J. Meteorol. Soc. Jpn., 96B, 27–42, https://doi.org/10.2151/jmsj.2018-001, 2018.

Joyce, R., Janowiak, J., and Huffman, G.: Latitudinally and Seasonally Dependent Zenith-Angle Corrections for Geostationary Satellite IR Brightness Temperatures, J. Appl. Meteorol., 40, 689, https://doi.org/10.1175/1520-0450(2001)040<0689:LASDZA>2.0.CO;2, 2001.

570 Karlsson, K.-G., Devasthale, A., and Eliasson, S.: Global Cloudiness and Cloud Top Information from AVHRR in the 42-Year CLARA-A3 Climate Data Record Covering the Period 1979–2020, Remote Sens., 15, 3044, 2023a.

Karlsson, K. G., Stengel, M., Meirink, J. F., Riihelä, A., Trentmann, J., Akkermans, T., Stein, D., Devasthale, A., Eliasson, S., Johansson, E., Håkansson, N., Solodovnik, I., Benas, N., Clerbaux, N., Selbach, N., Schröder, M., and Hollmann, R.: CLARA-A3: The third edition of the AVHRR-based CM SAF climate data record on clouds, radiation and surface albedo covering the 575 period 1979 to 2023, Earth Syst. Sci. Data, 15, 4901–4926, https://doi.org/10.5194/essd-15-4901-2023, 2023b.

Kawamoto, K., Nakajima, T., and Nakajima, T. Y.: A Global Determination of Cloud Microphysics with AVHRR Remote Sensing, J. Climate, 14, 2054–2068, https://doi.org/10.1175/1520-0442(2001)014<2054:AGDOCM>2.0.CO;2, 2001.

Knapp, K. R., Ansari, S., Bain, C. L., Bourassa, M. A., Dickinson, M. J., Funk, C., Helms, C. N., Hennon, C. C., Holmes, C. D., Huffman, G. J., Kossin, J. P., Lee, H.-T., Loew, A., and Magnusdottir, G.: Globally Gridded Satellite Observations for 580 Climate Studies, Bull. Am. Meteorol. Soc., 92, 893–907, https://doi.org/10.1175/2011BAMS3039.1, 2011.

Kocaman, S., Debaecker, V., Bas, S., Saunier, S., Garcia, K., and Just, D.: A comprehensive geometric quality assessment approach for MSG SEVIRI imagery, Adv. Space Res., 69, 1462–1480, https://doi.org/10.1016/j.asr.2021.11.018, 2022.

Letu, H., Ishimoto, H., Riedi, J., Nakajima, T. Y., C.-Labonnote, L., Baran, A. J., Nagao, T. M., and Sekiguchi, M.: Investigation of ice particle habits to be used for ice cloud remote sensing for the GCOM-C satellite mission, Atmos. Chem. 585 Phys., 16, 12287–12303, https://doi.org/10.5194/acp-16-12287-2016, 2016.

Letu, H., Yang, K., Nakajima, T., Ishimoto, H., Nagao, T., Riedi, J., Baran, A., Ma, R., Wang, T., Khatri, P., Chen, L., Shi, C., and Shi, J.: High-resolution retrieval of cloud microphysical properties and surface solar radiation using Himawari-8/AHI next-generation geostationary satellite, Remote Sens. Environ., 239, 1–16, https://doi.org/10.1016/j.rse.2019.111583, 2020a.

Letu, H., Yang, K., Nakajima, T. Y., Ishimoto, H., Nagao, T. M., Riedi, J., Baran, A. J., Ma, R., Wang, T., Shang, H., Khatri, 590 P., Chen, L., Shi, C., and Shi, J.: High-resolution retrieval of cloud microphysical properties and surface solar radiation using Himawari-8/AHI next-generation geostationary satellite, Remote Sens. Environ., 239, 111583, https://doi.org/10.1016/j.rse.2019.111583, 2020b.

Letu, H., Ma, R., Nakajima, T. Y., Shi, C., Hashimoto, M., Nagao, T. M., Baran, A. J., Nakajima, T., Xu, J., Wang, T., Tana, G., Bilige, S., Shang, H., Chen, L., Ji, D., Lei, Y., Wei, L., Zhang, P., Li, J., Li, L., Zheng, Y., Khatri, P., and Shi, J.: Surface 595 Solar Radiation Compositions Observed from Himawari-8/9 and Fengyun-4 Series, Bull. Am. Meteorol. Soc., 104, E1772–E1789, https://doi.org/10.1175/BAMS-D-22-0154.1, 2023.

Li, J., Pan, B., Zhang, F., Guo, B., Li, W., Jiang, G.-M., Wu, X., and Wang, Q.: Probabilistic Retrieval of All-Day Overlapping Cloud Microphysical Properties, Adv. Atmos. Sci., https://doi.org/10.1007/s00376-025-5234-7, 2025.

Li, J., Zhang, F., Li, W., Tong, X., Pan, B., Li, J., Lin, H., Letu, H., and Mustafa, F.: Transfer-Learning-Based Approach to Retrieve the Cloud Properties Using Diverse Remote Sensing Datasets, IEEE Trans. Geosci. Remote Sens., 61, 1–10, https://doi.org/10.1109/TGRS.2023.3318374, 2023a.2023.

Li, W., Zhang, F., Guo, B., Fu, H., and Letu, H.: Physics-Driven Machine Learning Algorithm Facilitates Multilayer Cloud Property Retrievals From Geostationary Passive Imager Measurements, IEEE Trans. Geosci. Remote Sens., 62, 1-18, https://doi.org/10.1109/TGRS.2024.3369621, 2024.

Li, W., Zhang, F., Lin, H., Chen, X., Li, J., and Han, W.: Cloud Detection and Classification Algorithms for Himawari-8 Imager Measurements Based on Deep Learning, IEEE Trans. Geosci. Remote Sens., 60, 1-17, https://doi.org/10.1109/TGRS.2022.3153129, 2022.

Li, W., Zhang, F., Lu, C., Jin, J., Shi, Y.-N., Cai, Y., Hu, S., and Han, W.: Integrated efficient radiative transfer model named Dayu for simulating the imager measurements in cloudy atmospheres, Opt. Express, 31, 15256-15288, https://doi.org/10.1364/OE.482762, 2023b.

Li, W., Zhang, F., Shi, Y. N., Iwabuchi, H., Zhu, M., Li, J., Han, W., Letu, H., and Ishimoto, H.: Efficient radiative transfer model for thermal infrared brightness temperature simulation in cloudy atmospheres, Opt. Express, 28, 25730-25749, https://doi.org/10.1364/oe.400130, 2020.

Liu, C., Zhang, F., Ouyang, H., Li, W., and Zhao, Z.: Diurnal Variation of Cloud Physical Properties for Tropical Cyclones Over North Atlantic in 2019–2023, Geophys. Res. Lett., 52, e2025GL115566, https://doi.org/10.1029/2025GL115566, 2025.

Liu, W. H., Yue, P., Wu, X. H., Li, J. J., Shao, N. F., Zhu, B., and Lu, C. S.: Why does a decrease in cloud amount increase terrestrial evapotranspiration in a monsoon transition zone?, Environ. Res. Lett., 19, https://doi.org/10.1088/1748-9326/ad3569, 2024.

Menzel, W. P., Frey, R. A., Zhang, H., Wylie, D. P., Moeller, C. C., Holz, R. E., Maddux, B., Baum, B. A., Strabala, K. I., and Gumley, L. E.: MODIS Global Cloud-Top Pressure and Amount Estimation: Algorithm Description and Results, J. Appl. Meteorol. Climatol., 47, 1175–1198, https://doi.org/10.1175/2007JAMC1705.1, 2008.

Min, M., Li, J., Wang, F., Liu, Z., and Menzel, W. P.: Retrieval of cloud top properties from advanced geostationary satellite imager measurements based on machine learning algorithms, Remote Sens. Environ., 239, 111616, https://doi.org/10.1016/j.rse.2019.111616, 2020.

Min, M., Wu, C., Li, C., Liu, H., Xu, N., Wu, X., Chen, L., Wang, F., Sun, F., Qin, D., Wang, X., Li, B., Zheng, Z., Cao, G., and Dong, L.: Developing the Science Product Algorithm Testbed for Chinese Next-Generation Geostationary Meteorological Satellites: Fengyun-4 Series, J. Meteorol. Res., 31, 708–719, https://doi.org/10.1007/s13351-017-6161-z, 2017.

Minnis, P. and Heck, P.: GOES-R Advanced Baseline Imager (ABI) Algorithm Theoretical Basis Document for Nighttime Cloud Optical Depth, Cloud Particle Size, Cloud Ice Water Path, and Cloud Liquid Water Path (Version 3.0), 85 pp., https://www.star.nesdis.noaa.gov/goesr/documents/ATBDs/Baseline/ATBD_GOES-R_Cloud_NCOMP_v3.0_Jul2012.pdf, 2012.

Mitra, A., Di Girolamo, L., Hong, Y., Zhan, Y., and Mueller, K. J.: Assessment and Error Analysis of Terra-MODIS and MISR Cloud-Top Heights Through Comparison With ISS-CATS Lidar, J. Geophys. Res. Atmos., 126, e2020JD034281, https://doi.org/10.1029/2020JD034281, 2021.

Mouri, K., Izumi, T., Suzue, H., and Yoshida, R.: Algorithm Theoretical Basis Document for Cloud Type/Phase Product, Meteorological Satellite Center Technical Note, 19–31, https://www.data.jma.go.jp/mscweb/technotes/msctechrep61-2.pdf, 2016.

Nakajima, T. and King, M. D.: Determination of the Optical Thickness and Effective Particle Radius of Clouds from Reflected Solar Radiation Measurements. Part I: Theory, J. Atmos. Sci., 47, 1878–1893, https://doi.org/10.1175/1520-0469(1990)047<1878:DOTOTA>2.0.CO;2, 1990.

Nakajima, T. Y. and Nakajma, T.: Wide-Area Determination of Cloud Microphysical Properties from NOAA AVHRR Measurements for FIRE and ASTEX Regions, J. Atmos. Sci., 52, 4043–4059, https://doi.org/10.1175/1520-0469(1995)052<4043:WADOCM>2.0.CO;2, 1995.

Pavolonis, M. J.: GOES-R Advanced Baseline Imager (ABI) Algorithm Theoretical Basis Document for Cloud Type and Cloud Phase (Version 2.0). 85 pp., https://www.star.nesdis.noaa.gov/goesr/documents/ATBDs/Baseline/ATBD_GOES-R_Cloud_Phase_Type_v2.0_Sep2010.pdf, 2010.

Platnick, S., Ackerman, S. A., King, M. D., Meyer, K., Menzel, W. P., Holz, R. E., Baum, B. A., and Yang, P.: MODIS atmosphere L2 cloud product (06_L2), NASA MODIS Adaptive Processing System, Goddard Space Flight Center [data set], Terra (MOD06_L2): 10.5067/MODIS/MOD06_L2.006, 2015.

650 Rossow, W. B. and Schiffer, R. A.: ISCCP Cloud Data Products, Bull. Am. Meteorol. Soc., 72, 2–20, https://doi.org/10.1175/1520-0477(1991)072<0002:ICDP>2.0.CO;2, 1991.

Rossow, W. B., Knapp, K. R., and Young, A. H.: International Satellite Cloud Climatology Project: Extending the Record, J. Climate, 35, 141–158, https://doi.org/10.1175/JCLI-D-21-0157.1, 2022.

Rossow, W. B., Walker, A. W., Beuschel, D. E., and Roiter, M. D.: International Satellite Cloud Climatology Project (ISCCP)
655 Documentation of New Cloud Datasets, World Meteorol. Organ., 1996.

Rossow, W. B., Mosher, F., Kinsella, E., Arking, A., Desbois, M., Harrison, E., Minnis, P., Ruprecht, E., Seze, G., Simmer, C., and Smith, E.: ISCCP Cloud Algorithm Intercomparison, J. Appl. Meteorol. Climatol., 24, 877–903, https://doi.org/10.1175/1520-0450(1985)024<0887:ICAI>2.0.CO;2, 1985.

Schiffer, R. A. and Rossow, W. B.: The International Satellite Cloud Climatology Project (ISCCP): The First Project of the
660 World Climate Research Programme, Bull. Am. Meteorol. Soc., 64, 779–784, https://doi.org/10.1175/1520-0477-64.7.779, 1983.

Shi, C., Letu, H., Nakajima, T. Y., Nakajima, T., Wei, L., Xu, R., Lu, F., Riedi, J., Ichii, K., Zeng, J., Shang, H., Ma, R., Yin, S., Shi, J., Baran, A. J., Xu, J., Li, A., Tana, G., Wang, W., Na, Q., Sun, Q., Yang, W., Chen, L., and Shi, G.: Near-global monitoring of surface solar radiation through the construction of a geostationary satellite network observation system, The
665 Innovation, 6, 100876, https://doi.org/10.1016/j.xinn.2025.100876, 2025.

Tang, C., Shi, C., Letu, H., Yin, S., Nakajima, T., Sekiguchi, M., Xu, J., Zhao, M., Ma, R., and Wang, W.: Development of a hybrid algorithm for the simultaneous retrieval of aerosol optical thickness and fine-mode fraction from multispectral satellite observation combining radiative transfer and transfer learning approaches, Remote Sens. Environ., 319, 114619, https://doi.org/10.1016/j.rse.2025.114619, 2025.

670 Tong, X., Li, J., Zhang, F., Li, W., Pan, B., Li, J., and Letu, H.: The Deep-Learning-Based Fast Efficient Nighttime Retrieval of Thermodynamic Phase From Himawari-8 AHI Measurements, Geophys. Res. Lett., 50, e2022GL100901, https://doi.org/10.1029/2022GL100901, 2023.

Trepte, Q. Z., Minnis, P., Sun-Mack, S., Yost, C. R., Chen, Y., Jin, Z., Hong, G., Chang, F. L., Smith, W. L., Bedka, K. M., and Chee, T. L.: Global Cloud Detection for CERES Edition 4 Using Terra and Aqua MODIS Data, IEEE Trans. Geosci.
675 Remote Sens., 57, 9410–9449, https://doi.org/10.1109/TGRS.2019.2926620, 2019.

Viggiano, M., Cimini, D., De Natale, M. P., Di Paola, F., Gallucci, D., Larosa, S., Marro, D., Nilo, S. T., and Romano, F.: Combining Passive Infrared and Microwave Satellite Observations to Investigate Cloud Microphysical Properties: A Review, Remote Sens., 17, 337, 2025.

Walther, A. and Heidinger, A. K.: Implementation of the Daytime Cloud Optical and Microphysical Properties Algorithm
680 (DCOMP) in PATMOS-x, J. Appl. Meteorol. Climatol., 51, 1371–1390, https://doi.org/10.1175/JAMC-D-11-0108.1, 2012.

Walther, A., Straka, W., and Heidinger, A. K.: GOES-R Advanced Baseline Imager (ABI) Algorithm Theoretical Basis Document for Daytime Cloud Optical and Microphysical Properties (DCOMP) (Version 3.0), 66 pp., https://www.star.nesdis.noaa.gov/goesr/documents/ATBDs/Baseline/ATBD_GOES-R_Cloud_DCOMP_v3.0_Jun2013.pdf, 2013.

685 Wang, M., Su, J., Han, X., Deng, X., Peng, N., and Liu, L.: Changes in Daytime Cirrus Properties From the ISCCP-H Data Set and Their Impacts on the Radiation Energy Budget, Earth Space Sci., 11, e2023EA003352, https://doi.org/10.1029/2023EA003352, 2024.

Winker, D., Pelon, J., Coakley, J., Ackerman, S., Charlson, R., Colarco, P., Flamant, P., Fu, Q., Hoff, R., Kittaka, C., Kubar, T., Treut, H., McCormick, M., Mégie, G., Poole, L., Trepte, C., Vaughan, M., and Wielicki, B.: The CALIPSO Mission: A
690 Global 3D View of Aerosols and Clouds, Bull. Am. Meteorol. Soc., 91, 1211–1230, https://doi.org/10.1175/2010BAMS3009.1, 2010.

Wu, X., Zhang, F., Zhang, H., Xiao, H., and Chen, G.: Deep Neural Network Based Scale-Adaptive Cloud Vertical Overlap Parameterization, Geophys. Res. Lett., 53, e2024GL112803, https://doi.org/10.1029/2024GL112803, 2026.

Xiao, H., Zhang, F., Zhang, R., Lu, F., Cai, M., and Wang, L.: Retrieval of Total Precipitable Water Under All-Weather
695 Conditions From Himawari-8/AHI Observations Using the Generative Diffusion Model, Geophys. Res. Lett., 52, e2025GL117075, https://doi.org/10.1029/2025GL117075, 2025a.

Xiao, H., Zhang, F., Wang, L., Pan, B., Zhu, Y., Wang, M., Li, W., Guo, B., and Li, J.: High-resolution ensemble retrieval of cloud properties for all-day based on geostationary satellite, npj Clim. Atmos. Sci., 8, 386, https://doi.org/10.1038/s41612-025-01263-x, 2025b.

700   Yang, C., Li, H., Zhu, R., Wang, Y., Zhang, F., Gu, M., Jiang, G.-M., Zhang, R., and Tang, X.: Snow or rain? hybrid AI deciphers surface precipitation phase from satellite observations, Nat. Commun., https://doi.org/10.1038/s41467-026-69487-w, 2026.

Yost, C. R., Minnis, P., Sun-Mack, S., Chen, Y., and Smith, W. L.: CERES MODIS Cloud Product Retrievals for Edition 4—Part II: Comparisons to CloudSat and CALIPSO, IEEE Trans. Geosci. Remote Sens., 59, 3695–3724,
705   https://doi.org/10.1109/TGRS.2020.3015155, 2021.

Young, A. H., Knapp, K. R., Inamdar, A., Hankins, W., and Rossow, W. B.: The International Satellite Cloud Climatology Project H-Series climate data record product, Earth Syst. Sci. Data, 10, 583–593, https://doi.org/10.5194/essd-10-583-2018, 2018.

Zhang, F., Zhu, M., Li, J., Li, W., Di, D., Shi, Y.-N., and Wu, K.: Alternate Mapping Correlated k-Distribution Method for
710   Infrared Radiative Transfer Forward Simulation, Remote Sens., 11, 994, https://doi.org/10.3390/rs11090994, 2019.

Zhang, H., Zhao, C., Li, J., Yu, Y., Chen, A., Yang, Y., Xia, Y., Yang, J., Sun, Y., Chi, Y., Zhao, X., Wang, Y., and Huang, J.: Shortwave cloud warming effect observed over highly reflective Greenland, Sci. Bull., 70, 951-959, https://doi.org/10.1016/j.scib.2025.01.027, 2025a.

Zhang, Q., Liu, C., Zhang, R., Yang, J., Li, J., Li, B., Lu, F., Yin, Y., and Jin, H.: Assessment of Geostationary Satellite Cloud
715   Effective Radius over East China with In Situ Aircraft Measurements, J. Meteorol. Res., 39, 240–251, https://doi.org/10.1007/s13351-025-4164-8, 2025b.

Zhang, Z., Dong, X., Xi, B., Song, H., Ma, P.-L., Ghan, S. J., Platnick, S., and Minnis, P.: Intercomparisons of marine boundary layer cloud properties from the ARM CAP-MBL campaign and two MODIS cloud products, J. Geophys. Res. Atmos., 122, 2351–2365, https://doi.org/10.1002/2016JD025763, 2017.

720   Zhao, L.: IRBT2CPP: A training and testing dataset for machine learning training, ranging from infrared brightness temperature to cloud physical properties, Science Data Bank [data set], doi:10.57760/sciencedb.27171, 2025.

Zhao, L., Zhang, F., Li, J., Lu, F., and Zhao, Z.: DaYu-GCP: DaYu all-day global cloud physical properties products with 0.07° resolution retrieved from geostationary satellite imagers covering the period from 2000 to 2022, Science Data Bank [data set], doi:10.57760/sciencedb.26292, 2026.

725   Zhao, Z., Zhang, F., Li, W., and Li, J.: Image-Based Retrieval of All-Day Cloud Physical Parameters for FY4A/AGRI and Its Application Over the Tibetan Plateau, J. Geophys. Res. Atmos., 129, e2024JD041032, https://doi.org/10.1029/2024JD041032, 2024.

Zhao, Z., Zhang, F., Wu, Q., Li, Z., Tong, X., and Li, J.: Cloud Identification and Properties Retrieval of the Fengyun-4A Satellite Using a ResUnet Model, IEEE Trans. Geosci. Remote Sens., 61, 1–18, https://doi.org/10.1109/TGRS.2023.3252023,
730   2023.